nIFTy galaxy cluster simulations – IV. Quantifying the influence of baryons on halo properties

Weiguang Cui,[1,2]★ Chris Power,[1,2] Alexander Knebe,[3,4] Scott T. Kay,[5]
Federico Sembolini,[3,4] Pascal J. Elahi,[6] Gustavo Yepes,[3,4] Frazer Pearce,[7]
Daniel Cunnama,[8] Alexander M. Beck,[9] Claudio Dalla Vecchia,[10,11]
Romeel Davé,[12,13,14] Sean February,[15] Shuiyao Huang,[16] Alex Hobbs,[17] Neal Katz,[16]
Ian G. McCarthy,[18] Giuseppe Murante,[19] Valentin Perret,[20] Ewald Puchwein,[21]
Justin I. Read,[22] Alexandro Saro,[9,23] Romain Teyssier[23] and Robert J. Thacker[24]

Affiliations are listed at the end of the paper

ABSTRACT

Building on the initial results of the nIFTy simulated galaxy cluster comparison, we compare and contrast the impact of baryonic physics with a single massive galaxy cluster, run with 11 state-of-the-art codes, spanning adaptive mesh, moving mesh, classic and modern smoothed particle hydrodynamics (SPH) approaches. For each code represented we have a dark-matter-only (DM) and non-radiative (NR) version of the cluster, as well as a full physics (FP) version for a subset of the codes. We compare both radial mass and kinematic profiles, as well as global measures of the cluster (e.g. concentration, spin, shape), in the NR and FP runs with that in the DM runs. Our analysis reveals good consistency ($\lesssim$20 per cent) between global properties of the cluster predicted by different codes when integrated quantities are measured within the virial radius R_{200}. However, we see larger differences for quantities within R_{2500}, especially in the FP runs. The radial profiles reveal a diversity, especially in the cluster centre, between the NR runs, which can be understood straightforwardly from the division of codes into classic SPH and non-classic SPH (including the modern SPH, adaptive and moving mesh codes); and between the FP runs, which can also be understood broadly from the division of codes into those that include active galactic nucleus feedback and those that do not. The variation with respect to the median is much larger in the FP runs with different baryonic physics prescriptions than in the NR runs with different hydrodynamics solvers.

Key words: methods: numerical – galaxies: clusters: general – galaxies: evolution – galaxies: formation – galaxies: haloes – cosmology: theory.

1 INTRODUCTION

The importance of galaxy clusters as probes of cosmology and testbeds for galaxy transformation and evolution is well recognized (e.g. Kravtsov & Borgani 2012). Numerical simulations are fundamental to give an accurate interpretation of the astrophysical processes observed in galaxy clusters (e.g. Borgani & Kravtsov 2011). Cosmological *N*-body simulations have been used to estimate the abundance of galaxy clusters as a function of redshift, which can be used to constrain values of the cosmological parameters such as σ_8 (e.g. Viel & Haehnelt 2006) and the dark energy equation of state

(e.g. Angulo et al. 2005), and to calibrate observational estimators of cluster mass (e.g. Fabjan et al. 2011; Kay et al. 2012; Munari et al. 2013) and sensitivity to dynamical state (e.g. Power, Knebe & Knollmann 2012).

Cosmological hydrodynamical simulations offer the potential to test galaxy transformation within cluster environments, although this has proven to be more challenging. The Santa Barbara Cluster Comparison (Frenk et al. 1999) already highlighted that simulations of the same object performed with different codes can produce divergent behaviour, most compactly quantified by the spherically averaged entropy profile – Eulerian mesh-based codes predicted entropy cores while Lagrangian smoothed particle hydrodynamics (SPH) codes predicted continuously declining entropy with decreasing radius. Subsequent studies demonstrated that this divergent

behaviour could be traced to the treatment of surface tension and the suppression of multiphase fluid mixing in the classic SPH codes (e.g. Wadsley, Veeravalli & Couchman 2008; Mitchell et al. 2009; Power, Read & Hobbs 2014; Sembolini et al. 2016).

Given the developments in astrophysical simulation codes, as well as the implementations of the hydrodynamic evolution of the baryons, after ∼15 yr of the Santa Barbara Cluster Comparison, it was natural to investigate how the state-of-the-art codes compared when faced with the same problem – that of the thermodynamical structure of a massive galaxy cluster at $z = 0$, when only gravity and non-radiative (NR) hydrodynamics is modelled. This formed the basis of the nIFTy galaxy cluster comparison, the first results of which were presented in Sembolini et al. (2016, hereafter Paper I). Initially, thirteen different codes – ART, AREPO, HYDRA, RAMSES and nine incarnations of GADGET – were used to simulate a massive galaxy cluster down to $z = 0$. The mesh-based codes ART and AREPO formed extended entropy cores in the gas with rising central gas temperatures, whereas 'classic' SPH codes produced falling entropy profiles all the way into the very centre with correspondingly rising mass profiles and central temperature inversions. In contrast, modern SPH codes produce gas entropy profiles that are essentially indistinguishable from those obtained with mesh-based codes.

Building on the work presented in Paper I, Sembolini et al. (2015, hereafter Paper II) compared these codes with different radiative physical implementations – such as cooling, star formation, and active galactic nucleus (AGN) feedback – and showed that adding radiative physics washes away the marked code-based differences present in the entropy profile seen in the NR simulations presented in Paper I.

Elahi et al. (2016, hereafter Paper III) found that subhalo properties are reasonably consistent across almost all codes in dark-matter-only (DM), NR, and full physics (FP) simulations, although the code-to-code scatter increases with the inclusion of gas and subgrid baryonic physics. In the FP runs, the synthetic galaxies that reside in these subhaloes show striking code-to-code variation, with differences in stellar and gas masses being up to 0.2–0.4 dex.

In this paper, we follow up on the results presented in Paper I, Paper II, Paper III, and focus on how the inclusion of the baryonic component modifies the spatial and kinematic structure of the simulated cluster. We seek to understand

(i) the scatter between simulation codes and different input baryon models; and

(ii) the effects of input baryon models on cluster properties, as well as the extent to which they converge.

We consider the global properties of the cluster – concentration, spin parameter, inner slope, masses, halo shapes, and velocity anisotropy. The cluster mass is calculated within the radii containing overdensities of 200, 500, and 2500 times the critical density of the Universe at $z = 0$ (i.e. R_{200}, R_{500}, R_{2500}). Halo shapes, as measured for isodensity and isopotential surfaces, and velocity anisotropy are calculated at these three radii. We also investigate the density, circular velocity, and velocity dispersion profiles.

The paper is organized as follows. In Section 2, we provide a brief summary of the main features of the astrophysical simulation codes used in this study, while in Section 3, we recall the key properties of the simulated galaxy cluster used in the comparison. The main results are presented in Sections 4 and 5, in which we investigate how the presence of a NR and radiative physical baryonic influences the simulated cluster. Finally in Section 6, we discuss our results and state our conclusions.

2 THE SIMULATION CODES

Following the classification adopted in nIFTy Paper I and Paper II, the 11 simulation codes used in this study are divided into four groups based on their gas dynamic solving techniques:

(i) Grid-based: – RAMSES (Teyssier 2002);
(ii) Moving-mesh: – AREPO (Springel 2010);
(iii) Modern SPH: – G2-ANARCHY (Dalla Vecchia et al., in preparation), G3-SPHS (Read & Hayfield 2012), G3-MAGNETICUM (Hirschmann et al. 2014), G3-X (Beck et al. 2016), G3-PESPH (Huang et al., in preparation); and
(iv) Classic SPH: – G3-MUSIC (Sembolini et al. 2013), G3-OWLS (Schaye et al. 2010), G2-X (Pike et al. 2014), HYDRA (Couchman et al. 1995).

For each simulation code we have DM runs and NR runs, which include both gas and dark matter particles; for a subset of the codes, we have FP runs, which include both stars, gas, and dark matter particles, and a range of baryonic physics, including gas heating and cooling, star formation, black hole (BH) growth, and various sources of feedback.

Following on from the findings presented in Paper I, we separate NR runs into two groups – those run with codes that recover declining entropy profiles with decreasing radius (classic SPH), which we refer to as 'Classic SPH', and those run with codes that recover entropy cores at small radii (mesh, moving mesh, and modern SPH), which we refer to as 'non-Classic SPH'. Further, we separate FP runs into runs with and without BH growth and AGN feedback (AGN and noAGN, respectively). The AGN feedback is believed to be essential for galaxy clusters, which can solve the overcooling problem, and provide better agreements with observational results (e.g. Puchwein, Sijacki & Springel 2008; Fabjan et al. 2010; Planelles et al. 2014; Planelles, Schleicher & Bykov 2015, and references therein). Although G3-PESPH does not directly include the AGN feedback, it uses the heuristic model (Rafieferantsoa et al. 2015) to quench star formation in massive galaxies, which can be viewed as mimicking AGN feedback. Thus, we include G3-PESPH in the AGN instead of noAGN subgroup. For reference, we list all simulation codes and implemented baryonic physics models in Table 1. We summarize the key features of the codes that are relevant for this study in Appendix A. We refer the reader to nIFTy Paper I, Paper II, and Paper III for a more detailed summary.

3 THE SIMULATED GALAXY CLUSTER

We use the same massive galaxy cluster simulated in Paper I, Paper II, and Paper III with a virial mass of $M_{200} \simeq 1.1 \times 10^{15} \, h^{-1} \, M_{\odot}$ and virial radius of $R_{200} \simeq 1.69 \, h^{-1}$ Mpc at $z = 0$.[1] This was selected from the MUSIC-2 sample (Sembolini et al. 2013, 2014; Biffi et al. 2014), a data set of hydrodynamical simulations of galaxy clusters that were re-simulated from the parent MultiDark[2] DM cosmological N-body simulation (Prada et al. 2012). In these simulations, cosmological parameters of $\Omega_M = 0.27$, $\Omega_b = 0.0469$, $\Omega_\Lambda = 0.73$, $\sigma_8 = 0.82$, $n = 0.95$, and $h = 0.7$ were assumed, in accordance with the *WMAP*7+ BAO+SNI data set presented in Komatsu et al. (2011).

---

[1] R_{200} is the radius within which the enclosed mean matter overdensity is 200 times the critical density of the Universe, while M_{200} is the total mass within R_{200}.
[2] www.cosmosim.org

Table 1. Brief summary of all the simulation codes participating in the nIFTy cluster comparison project.

Type	Code name, Reference	DM gravity solver	NR gas treatment	FP noAGN	AGN
			Baryonic models		
Grid-based	RAMSES, Teyssier (2002)	AMR	Godunov scheme with Riemann solver	N	Y
Moving-mesh	AREPO, Springel (2010)	TREEPM	Godunov scheme on moving mesh	Y[a]	Y[b]
	G2-ANARCHY, Dalla Vecchia et al. (in preparation)	TREEPM	SPH kernel: Wendland C2	N	N
	G3-SPHS, Read & Hayfield (2012)	TREEPM	Wendland C4	N	N
Modern SPH	G3-MAGNETICUM, Hirschmann et al. (2014)	TREEPM	Wendland C6	N	Y
	G3-X, Beck et al. (2016)	TREEPM	Wendland C4	N	Y
	G3-PESPH, Huang et al. (in preparation)	TREEPM	HOCTS B-spline	Y	N
	G3-MUSIC, Sembolini et al. (2013)	TREEPM	Cubic spline	Y[c]	N
Classic SPH	G3-OWLS, Schaye et al. (2010)	TREEPM	Cubic spline	N	Y
	G2-X, Pike et al. (2014)	TREEPM	Cubic spline	N	Y
	HYDRA, Couchman, Thomas & Pearce (1995)	AP^3M	Cubic spline	N	N

[a] This version is named AREPO-SH.
[b] This version is named AREPO-IL.
[c] Two versions (G3-MUSIC and G2-MUSICPI) are included in this model.

The initial conditions of all the clusters of the MUSIC-2 data set are publicly available.[3] Briefly, these were produced using the zooming technique described in Klypin et al. (2001). All particles within a sphere with a radius of $6\,h^{-1}$ Mpc around the centre of the halo in the parent MultiDark simulation at $z = 0$ were found in a low-resolution version (256^3 particles) of the parent, and mapped back to the parent's initial conditions to identify the Lagrangian region from which these particles originated. The initial conditions of the original simulations were generated on a finer mesh of size 4096^3. By doing so, the mass resolution of the re-simulated objects was improved by a factor of 8 with respect to the original simulations. In the high-resolution region the mass resolution for the DM simulations corresponds to $m_{DM} = 1.09 \times 10^9\,h^{-1}\,M_\odot$, while for the runs including a baryonic component, $m_{DM} = 9.01 \times 10^8\,h^{-1}\,M_\odot$ and $m_{gas} = 1.9 \times 10^8\,h^{-1}\,M_\odot$. In this paper, all the codes used the same aligned parameters (see the table 4 in Paper I) to re-simulate the selected cluster.

In our analysis, the cluster is first identified with AMIGA's-Halo-Finder (Gill, Knebe & Gibson 2004; Knollmann & Knebe 2009, AHF) and then its centre is defined as the position of the minimum of the gravitational potential (see Cui et al. 2016, for discussion about the agreement between different centre definitions). All the cluster properties, such as, spherical overdensity mass, radial profiles, are recalculated with respect to the minimum of the potential.

4 RADIAL PROFILES

4.1 Mass profiles

Visual impression: we begin by inspecting the differences in projected dark matter density between the DM and NR runs shown in Fig. 1, and between the DM and FP runs, shown in Fig. 2. Here, we show two examples from simulation codes drawn from the 'Classic SPH' and 'non-Classic SPH' subgroups – respectively, G3-MUSIC and AREPO. In practice, we use only the high-resolution dark matter particles within R_{200} and compute densities using a standard cubic spline SPH kernel with 128 neighbours at the position of each dark matter particle; these densities are then smoothed to a 2D mesh

---

(on x–y plane with a pixel size of $5\,h^{-1}$ kpc) using the same SPH kernel (Cui et al. 2014a, 2016). To show the projected dark matter density difference, these images are simply aligned with the cluster centre without further adjustment. The density change is given by $\delta_\rho = \rho_{NR,FP} - \rho_{DM}$; in Fig. 1, blue (red) indicates a negative (positive) δ_ρ, or depressed (enhanced) densities in the NR and FP runs with respect to the DM run. Note that dark matter particles have a slightly larger mass in DM runs than in the NR and FP runs; we compensate for this by correcting the dark matter particle mass in NR and FP runs to be the same as in the DM run.

Fig. 1 clearly shows that, at $z = 0$, dark matter density changes are normally within $0.5 \times 10^{15}\,h\,M_\odot\,Mpc^{-2}$ over all the cluster, except within the central regions and at the positions of satellites. In the centre, the dark matter density is depressed relative to the DM runs in the non-classic SPH runs, as shown in the AREPO panels, while the majority of classic SPH codes showed enhanced central densities, as shown in the G3-MUSIC panels. The density variations associated with substructures are also evident, especially at $z = 0$ associated with the large infalling substructure (to the bottom left) on the outskirts of the cluster, indicating that the inclusion of gas can introduce an offset in the timing of mergers between DM and NR runs. At redshift $z = 1$, differences in density are smaller than at $z = 0$, and the enhanced density within the central regions is evident in both subgroups of codes.

In Fig. 2, we show how the dark matter density changes between the DM and FP runs, and see similar trends as in Fig. 1. Interestingly, the additional baryonic processes, most likely gas cooling, in the FP runs compared to the NR runs result in obvious density contrasts within the central regions and in substructures. It is important to note at this point, and we shall make this clear in the remainder of the paper, that the split into the classic and non-classic SPH groupings is not really appropriate for the FP runs; there are large code-to-code variations within these subgroups, primarily driven by the baryon physics implementations.

Total enclosed mass profiles: in Fig. 3, we show how the enclosed total mass density profile varies between the NR and DM runs (left-hand column) and FP and DM runs (right-hand column) at $z = 0$ (upper panels) and $z = 1$ (lower panels). We use fixed size in logarithm for each radial bin. Within each panel, we show the radial profiles (upper section) and the residuals with respect to the median profiles (lower section). Vertical lines denote R_{2500} and

---

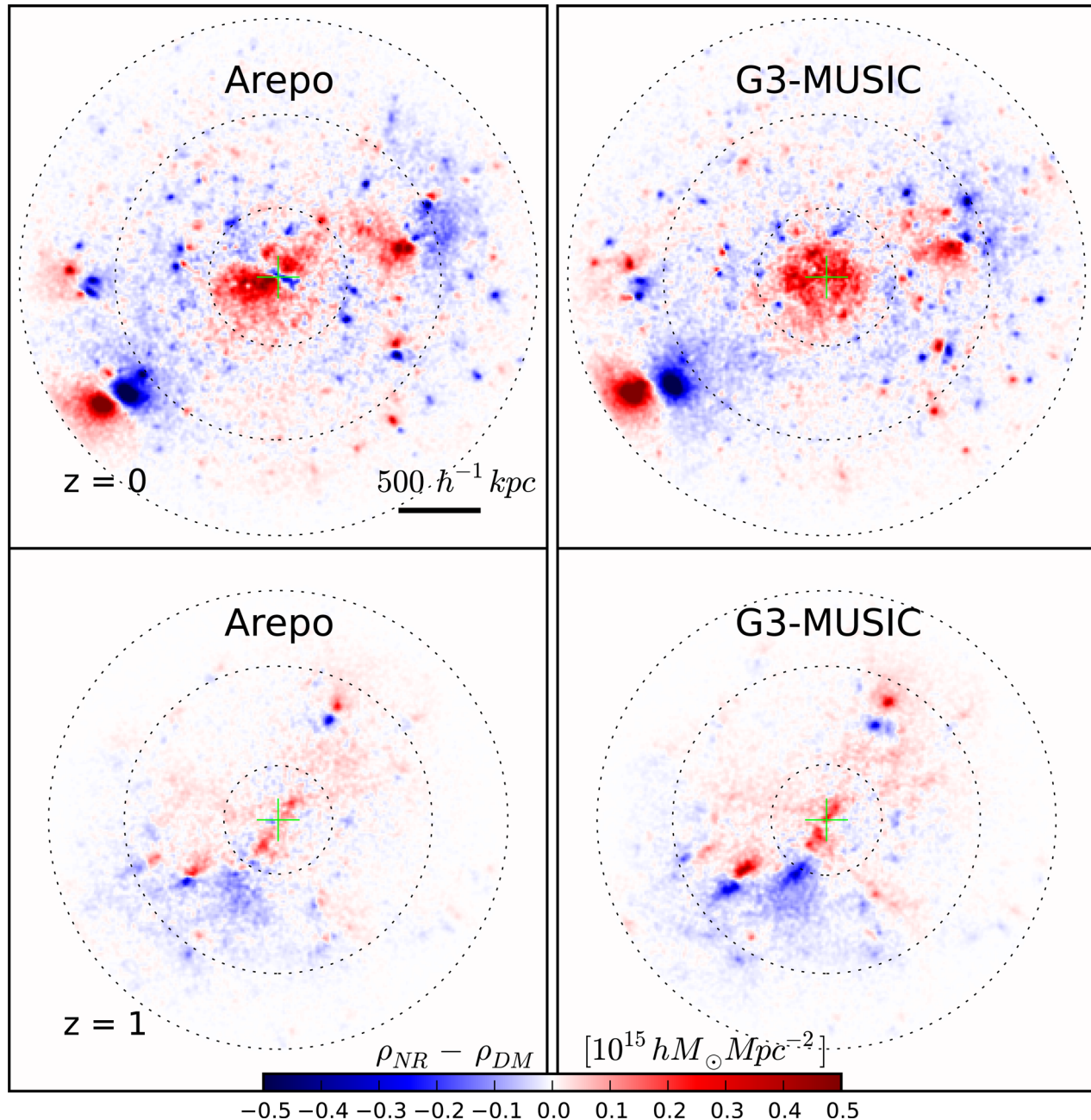[3] CLUSTER_00019 of the MUSIC-2 sample at http://music.ft.uam.es.

Figure 1. Projected dark matter density difference between DM and NR runs. We only show two simulation codes – AREPO and G3-MUSIC for illustration here. The colour is coding for the projected density difference, from negative values (blue) to positive values (red). The white region indicates no difference between the two runs. The simulation code name is shown on the top centre. The lime green cross in each plot indicates the aligned cluster centre position. The results in the upper (lower) row are from redshift $z = 0$ ($z = 1$). From inner to outer region, the three dotted circles represent R_{2500}, R_{500}, and R_{200} in the DM runs, respectively.

R_{500} measured in the fiducial G3-MUSIC DM (black dotted lines) and corresponding NR and FP runs (red and blue dashed lines, respectively). A lower cut of $R = 20 \, h^{-1}$ kpc, roughly in accordance with the convergence criterion presented in Power et al. (2003) has been applied. The data are separated according to the classic and non-classic SPH classification (thin and thick curves) in the case of the NR runs, and the AGN and noAGN classification (thick and thin curves) in the case of the FP runs.

We have already seen evidence in Fig. 1 that the dark matter density in the central regions of the cluster is depressed in the NR runs relative to the DM runs at $z = 0$. This depression is evident in

the total spherically averaged profiles; the non-classic SPH codes show densities of ∼80 per cent of their value in the DM run in the central regions of the cluster, while the classic SPH codes show a greater variation, ranging from a density of ∼80 per cent of the DM value for G3-MUSIC to ∼120 per cent for HYDRA. Similar behaviour as the classic SPH code – G3-MUSIC, has been reported in Cui et al. (2012); see Fig. 4 in this paper for more details.

The density is enhanced in the NR runs relative to the DM runs at large radii, outside of R_{2500}, in all of the codes. Interestingly, at $z = 1$, this trend of an enhancement in density continues to small radii, before plateauing and in some cases inverting, so that the density
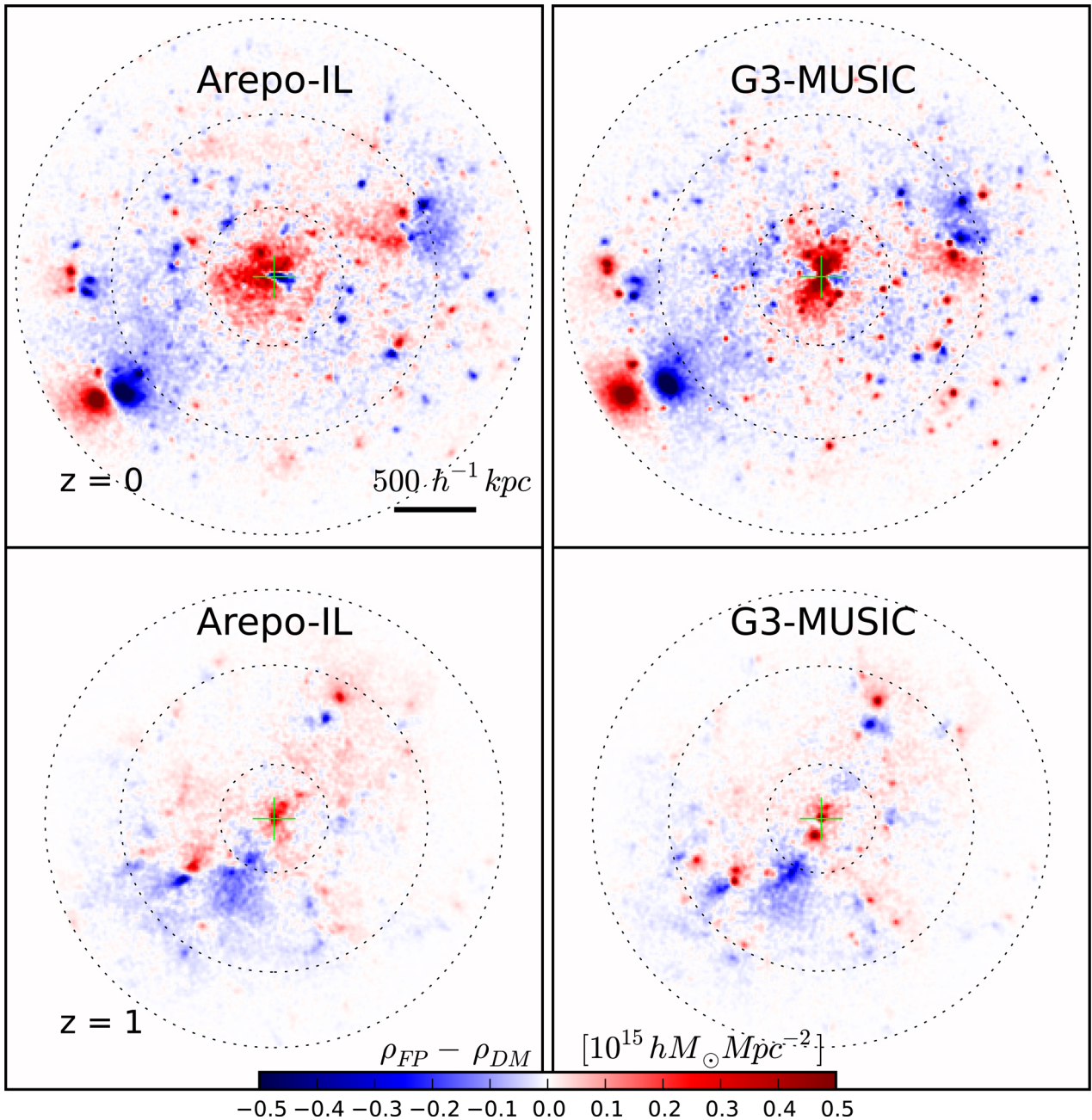
Figure 2. Projected dark matter density difference between DM and FP runs. Similarly to Fig. 1, we only show two sample simulation codes – AREPO-IL and G3-MUSIC here. Refer to Fig. 1 for the details.

is depressed in the NR run relative to the DM run; notably, the codes that invert and show density depressions relative to the DM run are all non-classic SPH codes. At $z = 1$, it is also noticeable that the variation between codes is large at small radii; the change is ∼20–50 per cent at 100 h^{-1} kpc. At $z = 0$, the variation is much smaller, ∼20 per cent at 100 h^{-1} kpc, ∼30 per cent if we include the outlier, HYDRA. The mesh code RAMSES shows larger increases respected to its DM run between R_{2500} and R_{500} than all the other codes at both $z = 0$ and 1. It means that this difference can be traced back to even high redshift. The non-classic SPH code G3-PESPH has the largest deviation with respect to other non-classic SPH codes. It shows a similar behaviour as the classic SPH code G2-X, which could be caused by a convergence issue (Read & Hayfield 2012).

To highlight the scatter between different codes, we show residuals with respect to the median for each of the non-classic SPH codes as individual curves in the lower panels, while we show residuals with respect to the median for the grouped classic SPH codes as the median (black dashed curves) and 1σ variation (shaded region). This shaded region is only indicating the scatter between the classic SPH codes. For example, its lower boundary does not mean that the classic SPH codes have the possibility of producing such low density. The disparity between the median values of the classic and non-classic SPH codes can be seen at $R \lesssim R_{2500}$ at both redshifts. The difference between the two subgroups is as large, if not larger, than the scatter between the codes within each subgroup; classic SPH codes tend to have roughly 20 per cent higher central densities
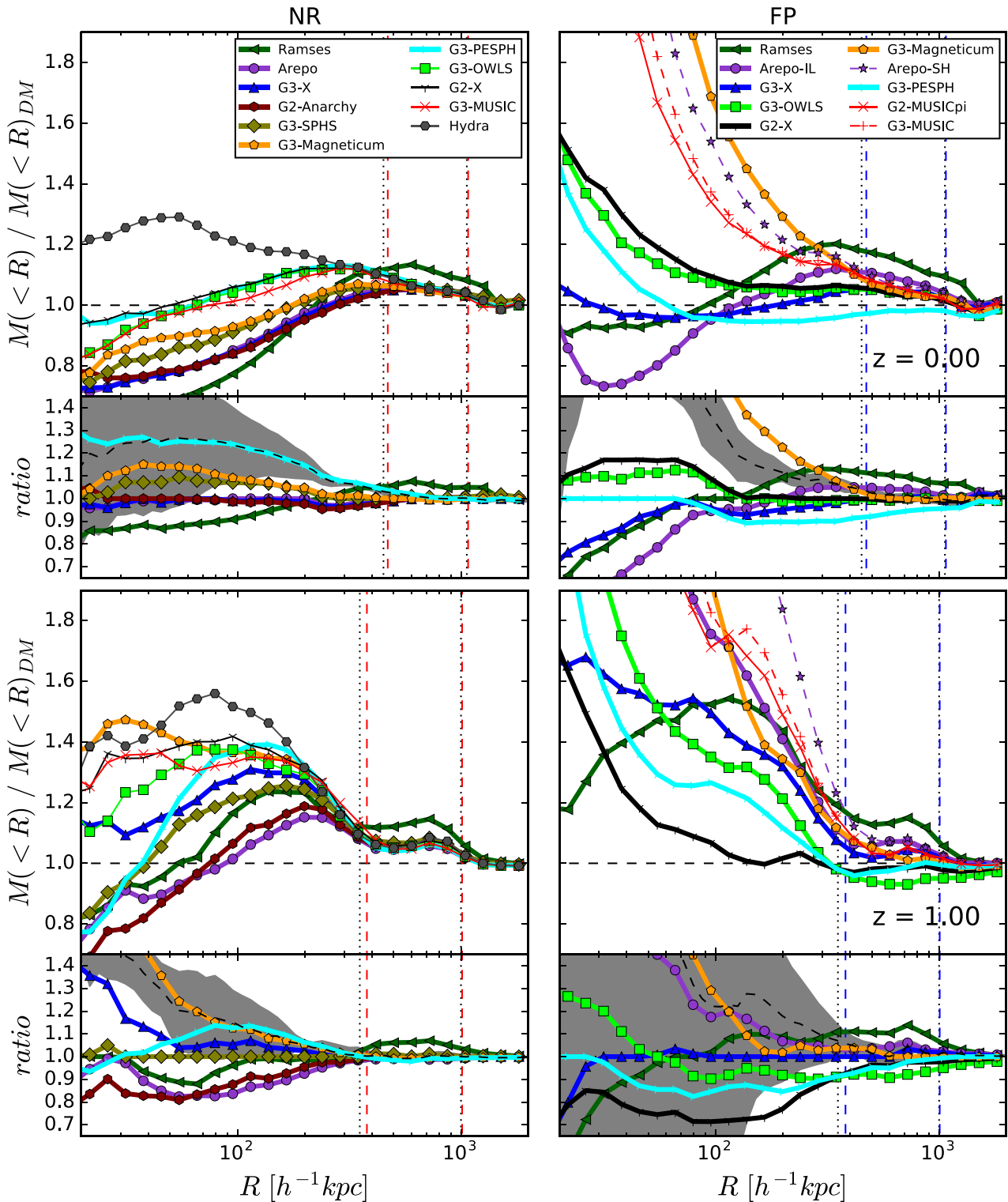
Figure 3. Differences in the cumulative mass profile between the NR/FP and DM runs. The left-hand column shows the difference between the mass profile in the NR and DM runs, while the right-hand column shows the corresponding result for the FP and DM runs. The line style, colour and symbol for each code are indicated in the legend. Vertical dashed (red for the NR runs; blue for the FP runs) lines show R_{2500} (inner) and R_{500} (outer) from the G3-MUSIC runs, while vertical dotted black lines are from the DM run. We show the results at $z = 0$ (top panel) and $z = 1$ (bottom panel). Under each plot, we show the residuals with respect to the median of the non-classic SPH density profiles (or the median profile of the AGN subgroup in the right-hand column), which are also shown in thick lines in the upper panels. The thin black dashed lines are the median profiles from classic SPH codes (or the median profiles from the noAGN subgroup in the right-hand column) with 1σ error shown by the shadow region. The classic SPH codes (also the noAGN codes in the right-hand column) in the upper panel are shown in thin lines.
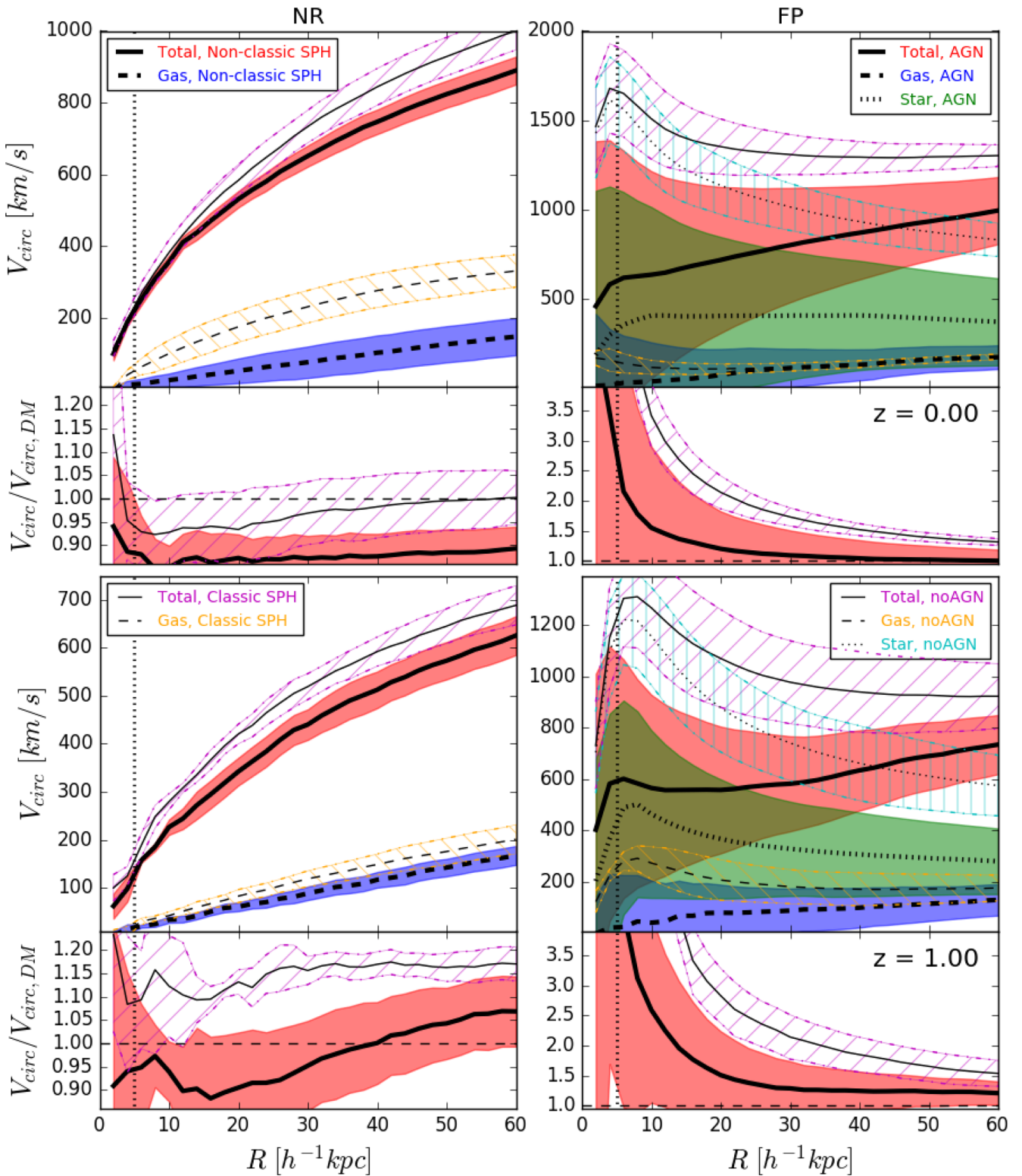
Figure 4. The circular velocity profile at the centre of the simulated cluster from NR runs (left-hand panel) and FP runs (right-hand panel). As indicated in the legends, the solid lines show the total circular velocity in the cluster centre; the dashed lines are the circular velocity from the gas component; the dotted lines are from the stellar component; the different coloured regions/hatchings and lines of different width show the standard deviation and median profile between different simulation codes in each subgroup, as indicated in the legends. The lower subplot below each main panel shows the total circular velocity difference between the NR/FP and DM runs. From top to bottom, we show the results at $z = 0$ and $z = 1$. The vertical dotted lines show the softening length in the simulation.

than non-classic SPH codes. It is worth to note here that the agreement between non-classic SPH codes at $z = 0$, can not be reached at $z = 1$, which shows a larger scatter $\sim$50 per cent.

The impact of baryonic physics on the total mass profile is particularly striking in the FP runs, with large variations between the different codes. At $z = 0$, the density within R_{2500} is enhanced in the majority of the codes, with only RAMSES, AREPO-IL and G3-X showing depressed densities. It is interesting that all three noAGN runs show increasing enhancements in relative density with decreasing radii, whereas there is no clear trend in the AGN runs, with some showing depressed relative central densities while others show strong enhancements. At $100\,h^{-1}$ kpc, the densities in the AGN runs relative to the DM runs vary between $\sim$100 per cent and $\sim$180 per cent, while the noAGN runs have relative densities varying between $\sim$130 per cent and $\sim$160 per cent. At $z = 1$, all of the runs show relative density enhancements within R_{2500}, ranging from $\sim$100 per cent to an excess of 200 per cent; as at $z = 0$, then we see that the three other noAGN runs show the largest relative enhancements at all radii. At $z = 0$, G3-MAGNETICUM produces the largest enhancement within R_{2500} in its FP run, however mimicking the behaviour of the other AGN codes in outer region and at redshift $z = 1$. This could be caused by the specific implementation of AGN feedback model, where BH merging and the parameters regulating the accretion on to the BH and the associated feedback are treated differently (see more details in Steinborn et al. 2015). Although G3-PESPH does not directly include the AGN feedback, it shows a similar behaviour as the AGN codes G2-X and G3-OWLS (see also in Paper I). This could be caused by its highly constrained heuristic model for galactic outflows (Davé et al. 2013), which utilizes outflows that scale as momentum-driven winds in sizeable galaxies.

The large variations in the behaviour of the curves in the AGN and noAGN runs with respect to the median, as shown in the residuals, emphasises the trends we have just noted. At $R \gtrsim R_{200}$, there is a good agreement between all of the codes for both AGN and noAGN runs; for $R_{200} \gtrsim R \gtrsim R_{2500}$, the differences become pronounced – up to $\sim$0–20 per cent – again regardless of whether or not they are AGN or noAGN. It is worth to note that the RAMSES still has the highest enhancement compared to the other codes as its NR run; while at $R \lesssim R_{2500}$, the variation with respect to the median is striking, especially in the case of the AGN runs. This is true at both $z = 0$ and $z = 1$.

These trends are consistent with the results of Martizzi et al. (2012), with mass profiles from the FP runs close to DM runs ($\lesssim$20 per cent) at radii $R \gtrsim 0.1 \times R_{200}$, and with Lin et al. (2006) and Cui et al. (2012), who also found lower relative central densities in the NR runs. The non-classic SPH codes tend to have lower central relative densities when compared to the classic SPH counterparts; because of gas pressure and energy redistribution between dark matter and gas particles during halo collapse, all the codes show a relative density enhancement at $R_{500} \gtrsim R \gtrsim 200\,h^{-1}$ kpc (this value is much smaller for the classic SPH codes and for the higher redshift). Similar results have been found in Rasia, Tormen & Moscardini (2004), Lin et al. (2006), and Cui et al. (2012).

The sensitivity of relative central densities to baryonic physics – of the kind implemented in the FP runs – has been reported previously (e.g. Duffy et al. 2010; Teyssier et al. 2011; Cui et al. 2012; Martizzi et al. 2012; Cui, Borgani & Murante 2014b; Velliscig et al. 2014; Schaller et al. 2015a). What is particularly interesting about our results is how much variation is evident in runs that seek to implement broadly similar baryonic physics prescriptions, especially at $z = 0$. Such variation is consistent with previous work; some studies report on enhancements in relative central densities, consistent

with the G2-X, G3-MAGNETICUM, and G3-OWLS AGN runs (e.g. Duffy et al. 2010; Cui et al. 2014b; Velliscig et al. 2014), while others report on relative central density depressions consistent with the RAMSES, AREPO-IL, and G3-XG3-X AGN runs (e.g. Teyssier et al. 2011; Martizzi et al. 2012). Understanding this variation is not straightforward – not only do the precise baryonic physics implementations differ, but there are also differences in the underlying scheme to solve the equations of gas dynamics, as the split between classic SPH codes, such as G2-X and G3-OWLS, and non-classic SPH codes, such as G3-MAGNETICUM and G3-X highlights.

4.2 Kinematic profiles

The previous results highlight that the inclusion of baryons has a significant impact on the mass distribution within the simulated cluster, especially within the central regions. We now investigate how this influences kinematic profiles.

Circular velocity: in Fig. 4, we show how the circular velocity profile within the cluster centre ($R \leq 60\,h^{-1}$ kpc) varies between the NR and DM runs (left-hand column) and FP and DM runs (right-hand column) at $z = 0$ (upper panels) and $z = 1$ (lower panels). We limit the profile within $60\,h^{-1}$ kpc because we are interesting in the core region of R_{2500}, where the profile is dominated by the brightest cluster galaxy in the FP sims. A fixed linear radial bin size is applied here. Within each panel, in the upper section we show the median profiles of the total matter (solid curves), gas (dashed curves), and, if present, stars (dotted curves), with the shaded regions and the hatchings between dot–dashed lines indicating the 1σ variation with respect to the median; in the lower section we show residuals with respect to the corresponding total matter profiles in the DM runs. Vertical lines denote a gravitational softening length of $5\,h^{-1}$ kpc, which was used in the DM and NR runs, and which is used as indicative of the softening in the FP runs. NR runs are grouped into non-classic SPH (thick lines with red shadow region) and classic SPH (thin lines with magenta shadow region), while FP runs are grouped into AGN (thick lines with red shadow region) and noAGN (thin lines with magenta shadow region) runs.

The residuals are particularly instructive. For the NR runs, at $z = 0$, there is a $\sim$1–5 per cent change in the total matter circular velocity in the classic SPH runs compared to DM runs, $\sim$10–15 per cent lower for the non-classic SPH runs; the change in circular velocity of the gas component between the classic and non-classic SPH runs is significant, in excess of 100 per cent. At $z = 1$, the classic SPH total matter circular velocity profile is $\sim$15 per cent higher than in the DM runs, whereas the non-classic SPH total circular velocity changes by between ~ -10 and $+10$ per cent from the inner to outer radius; the circular velocity profiles of the gas components are now much more in agreement with one another, differing by $\sim$10 per cent at most.

In the case of the FP runs, the impact of baryonic physics on the total matter circular velocity profile is substantial, with enhancements by factors of $\sim$1.5(3.5) at $10\,h^{-1}$ kpc and quickly decreasing to $\sim$0(40) per cent at $\sim$60$\,h^{-1}$ kpc, relative to the circular velocity profiles in the DM runs at $z = 0$ for the AGN (noAGN) subgroup. The enhancements are greatest for the noAGN runs, as we might expect – without the influence of the AGN, gas cooling can proceed relatively unhindered. There are significant differences between the stellar circular velocity profiles in the noAGN and AGN runs at both $z = 0$ and $z = 1$, by a factor of $\sim$2–3 over the radial range, whereas the differences between the gas circular velocity profiles are comparatively small – there is good consistency between the

AGN and noAGN runs at $z = 0$, although the noAGN profile is about tens of per cent higher than the AGN profile at $z = 1$.

Velocity dispersion profiles: as in Fig. 4, we show the total matter (solid line), gas (dashed line), and stellar (dotted line) velocity dispersion (σ) profiles from both NR and FP runs (left-hand and right-hand columns, respectively) in Fig. 5. In the upper (lower) panels we show results from $z = 0 (1)$, and in the upper (lower) section we show the differences with respect to the velocity dispersion profile in the corresponding DM run. The data is also binning in the same fixed linear size as in Fig. 4.

In the case of the NR runs, the total velocity dispersion profiles in the classic SPH and non-classic SPH runs are in very good agreement at $z = 0$ and reasonable agreement at $z = 1$. At $z = 0$, the difference with respect to the DM runs is small, with the ratio of $\sigma/\sigma_{\rm DM}$ of order unity; at $z = 1$, the difference is slightly greater, showing an enhancement by a factor of ~ 1.1–1.3 greater than in the DM run (greater within $\sim 10 \, h^{-1}$ kpc). The gas velocity dispersion profiles are broadly similar in the classic and non-classic SPH runs at both redshifts.

Against the circular velocity profiles in the FP runs, here we see a less significant variation in the velocity dispersion profiles with respect to the median, evident in Fig. 5. At $z = 0$, the median total matter and stellar velocity dispersions have a broadly similar shape and amplitude, albeit with the noAGN velocity dispersions being larger; the gas profiles show a slightly larger discrepancy, although both are flat over most of the radial range, and here the AGN velocity dispersion is larger, as we might expect in the presence of feedback from the central AGN. Relative to the DM runs velocity dispersion profiles, we see that the ratio with respect to both AGN and noAGN is flat and of order unity in the AGN runs and ~ 1.1 in the noAGN runs. Both sets of runs show a decline within the central $\sim 10 \, h^{-1}$ kpc. At $z = 1$, the total matter velocity dispersion in the AGN runs rises sharply in the inner regions before flattening off at $R \gtrsim 30 \, h^{-1}$ kpc, whereas the noAGN case shows a steady increase with increasing radius. The difference with respect to the DM run is shown in the lower section, and we see that the ratio in both the AGN and noAGN runs is flat at $R \gtrsim 20 \, h^{-1}$ kpc and corresponds to an enhancement by a factor of ~ 1.2, but shows a smaller enhancement in the AGN run and a slightly larger enhancement in the noAGN run at $R \lesssim 20 \, h^{-1}$ kpc. The gas velocity dispersion profiles show an inversion of the behaviour evident at $z = 0$ with large difference; while the stellar velocity dispersion differences between the median values from the AGN and noAGN groups are smaller compared to the $z = 0$ result.

The circular velocities for the gas, stellar, and total components from the AGN subgroup are similar to the results from Schaller et al. (2015a, see the most massive groups in the Fig. 6 for details). By comparing their NR simulation with the one including gas cooling and stellar feedback, Lau, Nagai & Kravtsov (2010) showed that the baryon dissipation increases the velocity dispersion of dark matter within the virial radius by ≈ 5–10 per cent. This effect is mainly driven by the changes of the density and gravitational potential in inner regions of cluster. Their explanation for the changes in the velocity dispersion is explicitly shown in Fig. 5.

5 GLOBAL PROPERTIES

5.1 Enclosed mass

As we saw in Fig. 3, there are mass profile changes at R_{2500}, R_{500}, and R_{200}. These changes are directly connected to the spherical overdensity (SO) halo mass. In Fig. 6, we show how the measured

SO masses – from left to right, M_{2500}, M_{500}, and M_{200} – vary with respect to the DM run in the NR runs (left-hand column) and FP runs (right-hand column) at $z = 0$ (upper panels) and $z = 1$ (lower panels). The meaning of the different coloured symbols is indicated in the insets.

The change in M_{200} is negligible; $M_{\rm NR, FP}/M_{\rm DM} \approx 1$ with whiskers indicating variations of ± 2 per cent at both redshifts, independent of code used or baryonic physics implemented. The change in $M_{500, \rm NR}$ is already slightly larger, ~ 5 per cent compared to $M_{500, \rm DM}$, at both redshifts; there is good consistency between codes in the classic SPH and non-classic SPH, and AGN and noAGN subgroups, although the scatter is larger in the FP runs. At the highest overdensity, M_{2500}, we see the greatest mass increase with very large error bars for both the NR and FP runs and median enhancements of ~ 10–20 per cent. In the NR runs, there is a clear separation in the medians at both $z = 0$ and 1 between the classic and non-classic SPH runs, with the larger change in the classic SPH runs, as the results so far imply; the variation with respect to the median is smaller in the classic SPH runs, but it never exceeds ~ 10 per cent. In the FP runs, there is a large variation with respect to the median in both the AGN and noAGN runs at both $z = 0$ and 1, in excess of $\sim 10(20)$ per cent at $z = 0 (1)$; again, the trend is as we would expect, with the noAGN runs having larger values of M_{2500}, arising from enhanced gas cooling and star formation in the core.

The influence of baryonic physics on mass has been investigated by a number of authors (e.g. Gnedin et al. 2004; Stanek, Rudd & Evrard 2009; Cui et al. 2012, 2014b; Sawala et al. 2013; Balaguera-Antolínez & Porciani 2013; Di Cintio et al. 2014a,b; Cusworth et al. 2014; Martizzi et al. 2014; Velliscig et al. 2014; Chan et al. 2015; Khandai et al. 2015; Schaller et al. 2015a; Bocquet et al. 2016; Zhu et al. 2016). Our results are consistent with the findings of Cui et al. (2012, see Fig. 2 for more details), and in particular, the insensitivity of M_{200} to simulation code and precise baryonic model is in broad agreement with previous studies (cf. the work of Cui et al. 2014b; Schaller et al. 2015a, who focused on cluster mass scales).

5.2 Central density profile

Following Newman et al. (2013) and Schaller et al. (2015b), we characterize the central total mass density profile by the average logarithmic slope over the radial range $0.003R_{200}$ to $0.03R_{200}$,

$$\gamma = - < \frac{d \log \rho_{\rm tot}(r)}{d \log r} >, \tag{1}$$

here we used 25 equally spaced logarithmic bins to construct the density profile. We have verified that the number of bins has little effect on the γ value as long as it is larger than 10. The results are shown in Fig. 7 and reveal some interesting trends.

First, the average slope in the NR runs increases from $\gamma_{\rm NR} \simeq 0.7$ at $z = 1$ to $\gamma_{\rm NR} \simeq 0.8$ at $z = 0$, while the variation in $\gamma_{\rm NR}$ with respect to the mean decreases by a factor of a few between $z = 1$ and $z = 0$.

Secondly, the ratio of the average slope in the NR runs with respect to the DM runs shows little variation with redshift – $\langle \gamma_{\rm NR}/\gamma_{\rm DM} \rangle \simeq 1$ for the non-classic SPH runs, $\langle \gamma_{\rm NR}/\gamma_{\rm DM} \rangle \simeq 0.9$ for the classic SPH runs – whereas the variation with respect to the mean shows a sharp decrease between $z = 1$ and $z = 0$, by a factor of several.

Thirdly, there is a large spread in slopes in the FP runs, ranging from $\gamma_{\rm FP} \simeq 1$ to 3, at both $z = 0$ and $z = 1$; separating runs into those with and without AGN and taking the average reveals no difference at $z = 1$ ($\langle \gamma_{\rm FP} \rangle \simeq 2.2$ for both AGN and noAGN runs), whereas
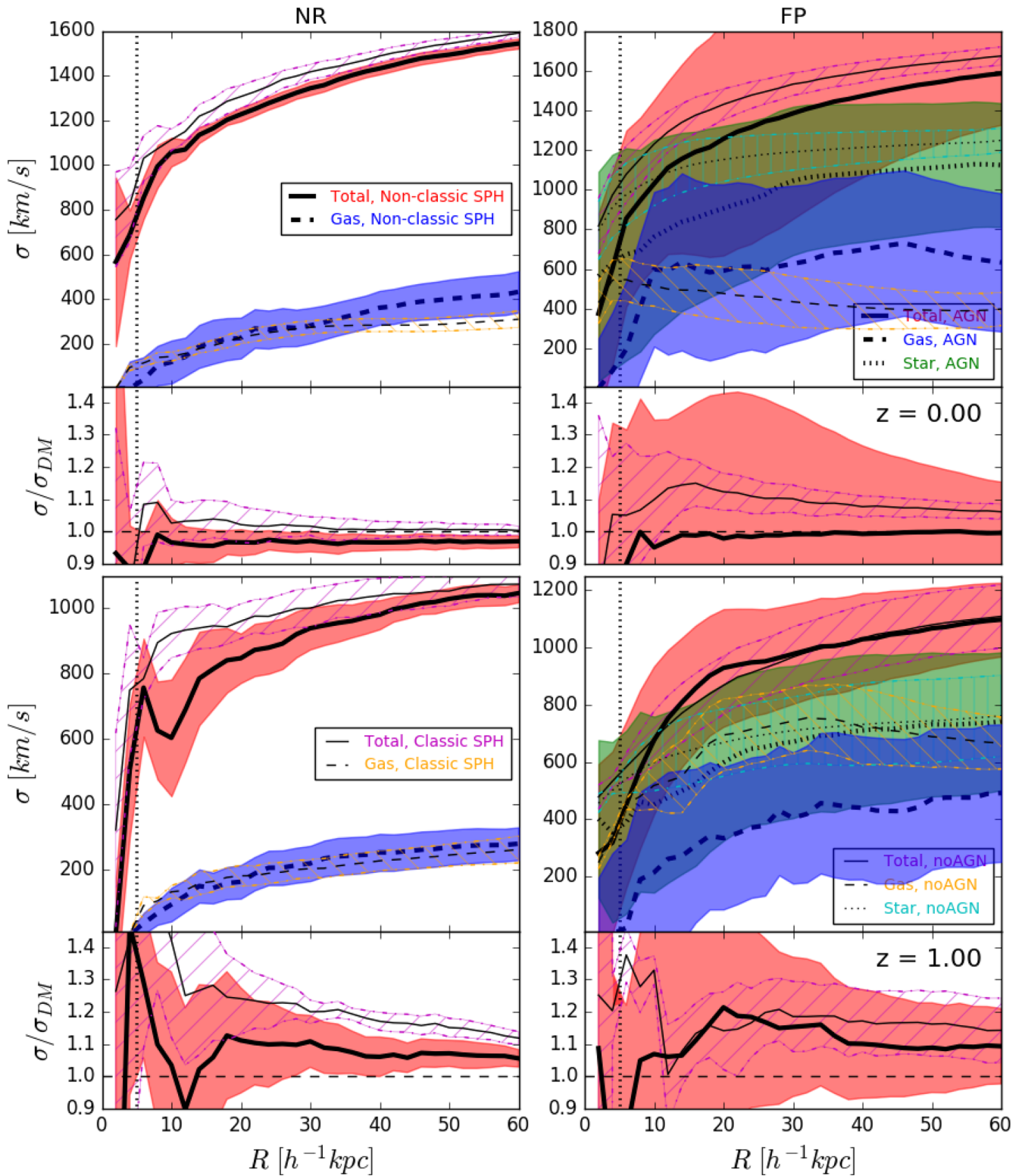
Figure 5. Similarly to Fig. 4, but for the velocity dispersion profile at the centre of the simulated cluster. Refer to Fig. 4 for more details of the subplot distributions and to the legends for the line styles and coloured region/hatching meanings.

there is a reasonably significant difference at $z = 0$ ($\langle \gamma_{FP} \rangle \simeq 1.5$ for AGN runs, $\langle \gamma_{FP} \rangle \simeq 2.2$ for noAGN runs) and in the sense we might expect (i.e. steeper slopes in the noAGN runs, indicating enhanced star formation and cold gas in the central galaxy). The median value from the AGN runs is slightly higher than the result from Schaller

et al. (2015b). However, it is slightly smaller than the result from Remus et al. (2013), which predicted the slope of $\gamma_{total} \approx 2$ within half mass radius.

Fourthly, there are dramatic enhancements in the average slope in the FP runs with respect to the DM runs, with $\langle \gamma_{FP} / \gamma_{DM} \rangle \simeq 2$ at
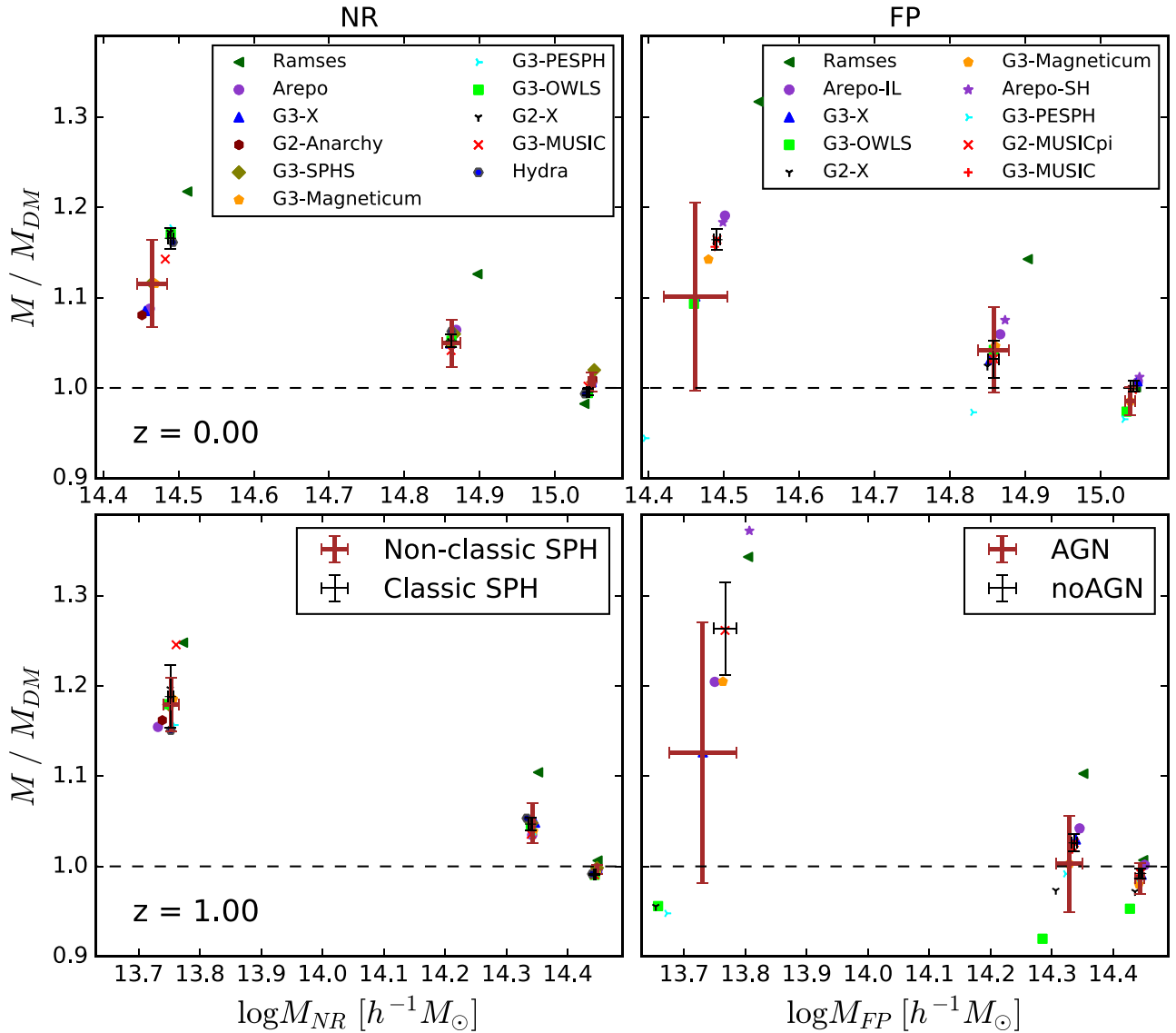
Figure 6. Halo mass difference between the DM runs and the NR runs (left-hand column)/the FP runs (right-hand column). As indicated in the legends in the top row, different coloured symbols indicate different simulation codes. In each panel, there are three groups of data with error bars, which correspond to M_{2500}, M_{500}, and M_{200} from smaller to larger halo mass. The meaning of the error bars in both columns is shown in the legends in the two lower panels: the brown thick one is for the non-classic SPH subgroup (AGN subgroup in the right-hand column); while the black thin error bar is for the classic SPH subgroup (noAGN subgroup in the right-hand column). From top to bottom panel, we show the results at $z = 0$ and 1, respectively.
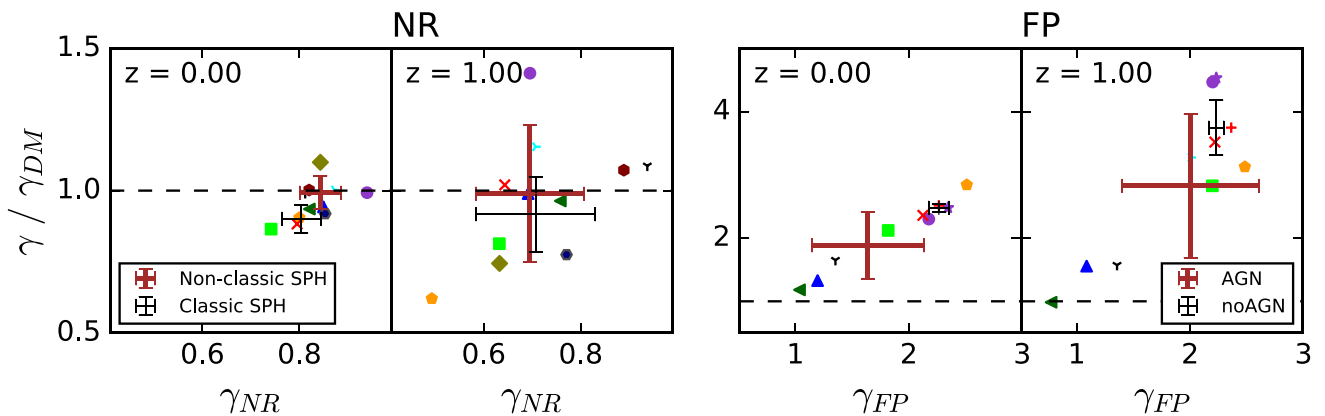
Figure 7. The inner slope changes for the NR runs (left-hand panel) and the FP runs (right-hand panel). The coloured symbols represent the different simulation codes as in Fig. 6. The meaning of the error bars are shown in the legends in both left-hand and right-hand panels.

$z = 0$ and $\langle\gamma_{FP}/\gamma_{DM}\rangle \simeq 3$–4 at $z = 1$, and as in the NR runs, the variation with respect to these averages shrinks by a factor of ~2–3 between the AGN and noAGN runs at both redshifts.

5.3 Concentration

The results so far suggest that there should be a measurable difference in the concentration parameter between the different sets of runs. We investigate this by assuming that the spherically averaged dark matter density profile, $\rho(r)$, can be approximated by the Navarro, Frenk & White (1996, 1997) form,

$$\frac{\rho(r)}{\rho_{\mathrm{crit}}} = \frac{\delta_c}{(r/r_s)(1 + r/r_s)^2}, \tag{2}$$

here ρ_{crit} is the critical density of the Universe, δ_c a characteristic density, and r_s a characteristic radius that is directly related to the concentration $c_{\mathrm{NFW}} = R_{200}/r_s$.

There is an extensive literature on the accuracy with which equation (2) describes density profiles in DM simulations, and while it represents a reasonable approximation to the ensemble averaged density profile of dark matter haloes in dynamical equilibrium, it cannot capture the shape of the density profile in detail. The presence of baryons complicates matters even further, as shown by Schaller et al. (2015a), but equation (2) provides a reasonable description of the dark matter density profile over the radial range $[0.05R_{200}$–$R_{200}]$.

Following Schaller et al. (2015a), we fit both NFW parameters (i.e. δ_c and r_s) to the dark matter density profile within this radial range in the DM, NR, and FP runs, using the CURVE_FIT package from SCIPY with equally spaced logarithmic bins. In Fig. 8, we show residuals corresponding to these NFW fits using data drawn from the classic and non-classic SPH examples, G3-MUSIC and AREPO; solid, dashed, and dotted lines indicate DM, NR, and FP runs. Note that there are two versions of the FP runs for each code. Within the fitting radius range, which is indicated by the thick lines, the dark matter component mass profile agrees with the NFW profile to within ~15 per cent (slightly worse at $z = 1$) for all three baryonic models.

In Fig. 9, we show how the ratio of concentration in the NR and FP runs (left-hand and right-hand panels) relative to the DM run varies with measured concentration. Within each panel, the left (right) section shows the $z = 0$ (1) trend. The behaviour in both the NR and FP runs is similar. At $z = 0$, the concentration is enhanced in both the classic and non-classic SPH runs, and in the AGN and noAGN runs, to a similar extent, a factor of ~1–1.2. At $z = 1$, the enhancements are more pronounced in all of the NR and FP runs, a factor of ~1.5, although the spread in values is larger in the FP runs. Interestingly, for the NR runs at $z = 0$, we see a clear separation in the median value and enhancement of the concentration, with the classic SPH runs showing a higher concentration and enhancement, consistent with our observations in the previous section.

The concentration enhancements in the NR runs and the noAGN FP runs are consistent with Duffy et al. (2010) and Fedeli (2012). The increased concentration found in the FP runs with AGN feedback is in agreement with Schaller et al. (2015a), but contradicting Duffy et al. (2010), who found either no change or a decrement in concentration. We caution that our small number statistics may play a role in the difference.

5.4 Spin parameter

The spin parameter λ is commonly used to quantify the degree to which the structure of a system is supported by angular momentum.

Several definitions for spin have been proposed, but we investigate the two most common definitions;

(i) λ_P, the dimensionless 'classical' spin parameter (Peebles 1969),

$$\lambda_P = \frac{J\sqrt{|E|}}{GM^{5/2}}, \tag{3}$$

where J is the magnitude of the angular momentum of material within the virial radius, M is the virial mass, and E is the total energy of the system; and

(ii) λ_B, the modified spin parameter of Bullock et al. (2001), which avoids the expensive calculation of the total energy E of a halo,

$$\lambda_B = \frac{J}{\sqrt{2}MVR}, \tag{4}$$

here $V = \sqrt{GM/R}$ is the circular velocity at the virial radius R, and M and J have the same meaning as in the 'classical' spin parameter λ_P. Both spin parameters are calculated including all material with $r \leq R_{200}$.

The spin parameters measured in the NR and FP runs are shown in the left-hand and right-hand panels, respectively, of Fig. 10; coloured symbols are as in Fig. 6. FP runs are grouped into AGN (brown thick error bars) and noAGN models (black thin error bars); NR runs are separated into non-classic (brown thick error bars) and classic SPH (black thin error bars) runs.

There are a couple of points worthy of note in this figure. First, there is a systematic drop between $z = 1$ and $z = 0$ in the ratio of λ_B and λ_P with respect to their DM counterparts in both the NR and FP runs and in all of the groupings (classic versus non-classic SPH, AGN versus noAGN). Secondly, the measured spins are broadly similar in the NR runs, independent of either redshift or classic versus non-classic SPH grouping, but there is a much larger spread in values in the FP runs, and the result is sensitive to whether or not AGN is included.

Interestingly, Bryan et al. (2013) found that the $z = 0$ spin distribution of dark matter haloes extracted from runs including baryonic physics, both with and without AGN feedback, is not significantly different from that of DM haloes. They reported that their baryon runs exhibit slightly lower median spin values at $z = 2$ than in their DM runs, in apparent contradiction to our results. However, their median halo mass is $M_{200} = 2 \times 10^{12}\,h^{-1}\,\mathrm{M}_\odot$, which is about three orders lower than our cluster, and these systems will have significantly different merging histories than our cluster. Merging history is likely to influence the angular momentum content of the system, especially that of the gaseous component, with angular momentum cancellation occurring in response to collisions and shocks of gas from multiple infall directions.

5.5 Shape of isodensity and isopotential shells

Having considered the spin parameter, we now move on to the shape of the cluster's isodensity and isopotential surfaces. We adopt the common method of diagonalization of the inertia tensor and characterization with ellipsoids of either the interpolated density field (e.g. Jing & Suto 2002) or the underlying gravitational potential (e.g. Springel, White & Hernquist 2004; Hayashi, Navarro & Springel 2007; Warnick, Knebe & Power 2008). Following Bett et al. (2007) and Warnick et al. (2008), the inertia tensor (see Warnick et al.
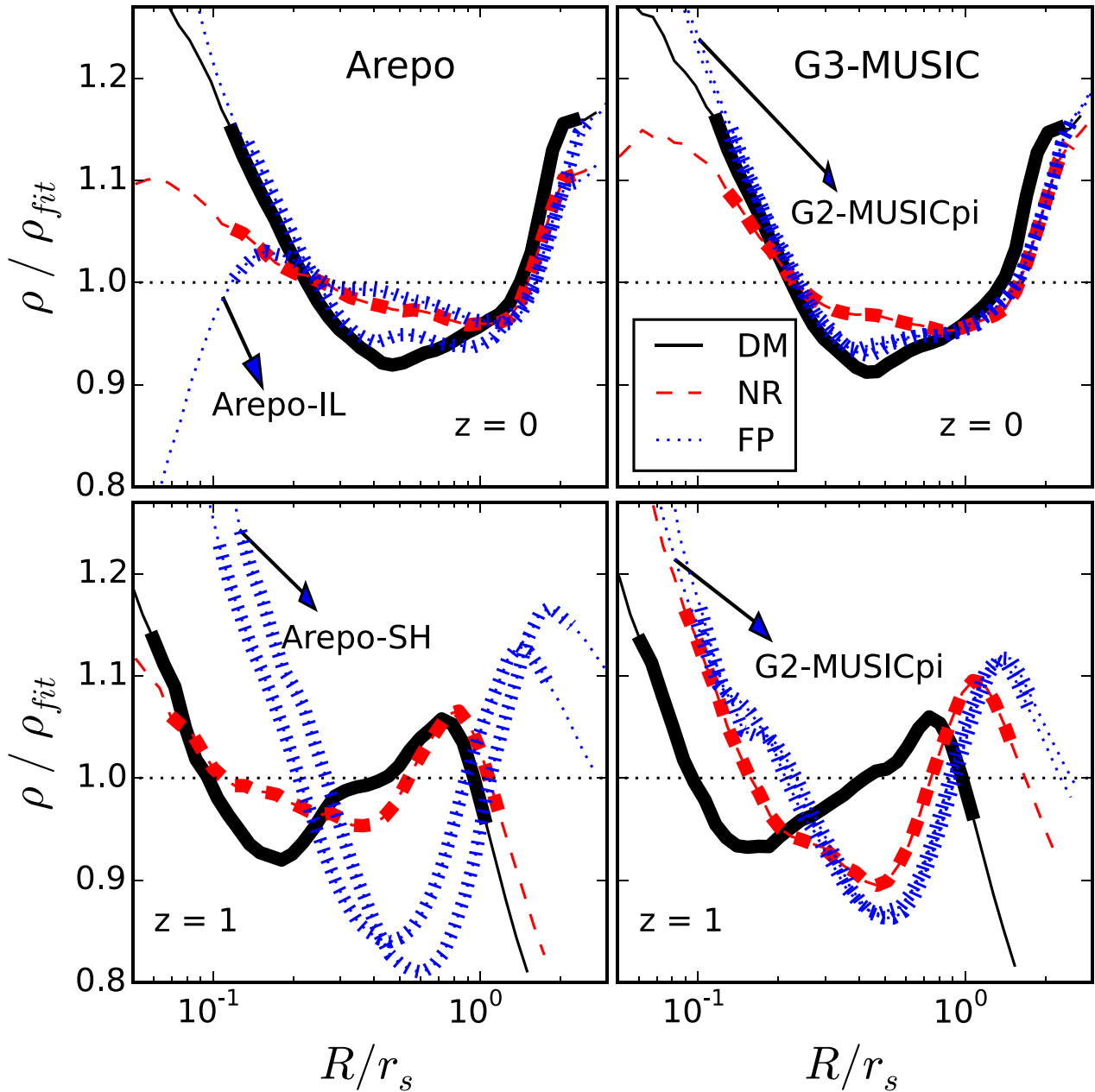
Figure 8. Mass profile ratio to the NFW fitting for the dark matter component as a function of radius, which is normalized to the fitted parameter r_s. Similarly to Fig. 1, we only illustrate two example simulations at here. The simulation code names are shown in the top of each panel. Different colour and style lines represent different baryonic models as indicated in the legend of the top-right panel. The thick lines indicate the region used for the NFW fitting. Upper row shows the result at $z = 0$, while the lower row is the result at $z = 1$.

2008; Vera-Ciro et al. 2011, for more discussions of the choice of inertia tensor) is defined as

$$I_{\alpha\beta} = \sum_{i=1}^{N} m_i (r_i^2 \delta_{\alpha\beta} - x_{i,\alpha} x_{i,\beta}), \tag{5}$$

where r_i is the position vector of the ith particle, α and β are tensor indices ($\alpha, \beta = 1, 2, 3$), $x_{i,\alpha}$ are components of the position vector of ith particle, and $\delta_{\alpha\beta}$ is the Kronecker delta. We estimate the shape of isodensity and isopotential shells at three radii: R_{2500}, R_{500}, and R_{200}, selecting all particles (including dark matter, star, and

gas components) within these shells as described in Appendix B. Eigenvalues can be computed by noting that

$$I = \frac{M}{5} \begin{bmatrix} b^2 + c^2 & 0 & 0 \\ 0 & a^2 + c^2 & 0 \\ 0 & 0 & a^2 + b^2 \end{bmatrix}. \tag{6}$$

These axes then describe a hypothetical uniform ellipsoid whose axes $a \geq b \geq c$ are those of the halo itself. Thus, we can have $b/a = \sqrt{(I_a + I_c - I_b)/(I_b + I_c - I_a)}$ and $c/a = \sqrt{(I_a + I_b - I_c)/(I_b + I_c - I_a)}$. For completeness, we also use a direct linear least-squares fitting method to fit ellipsoids to the 3D
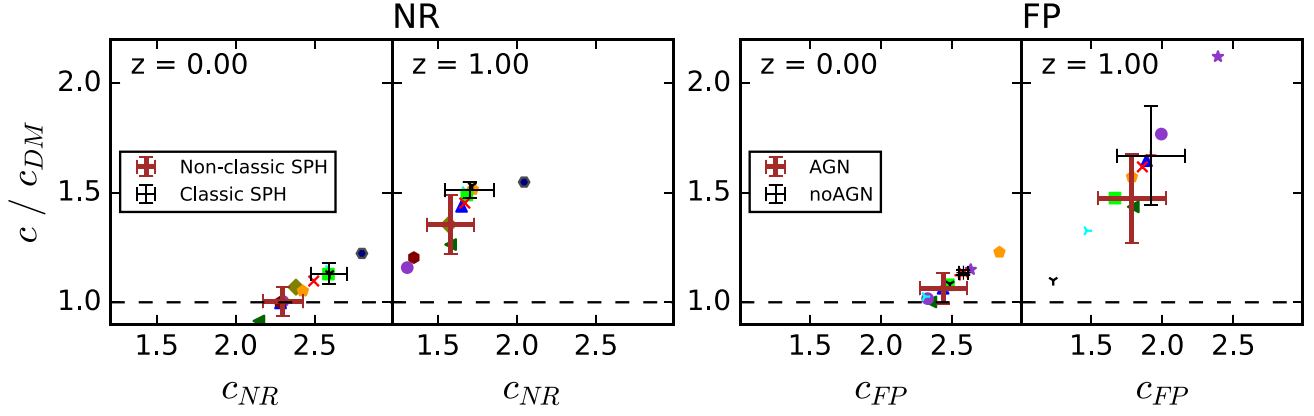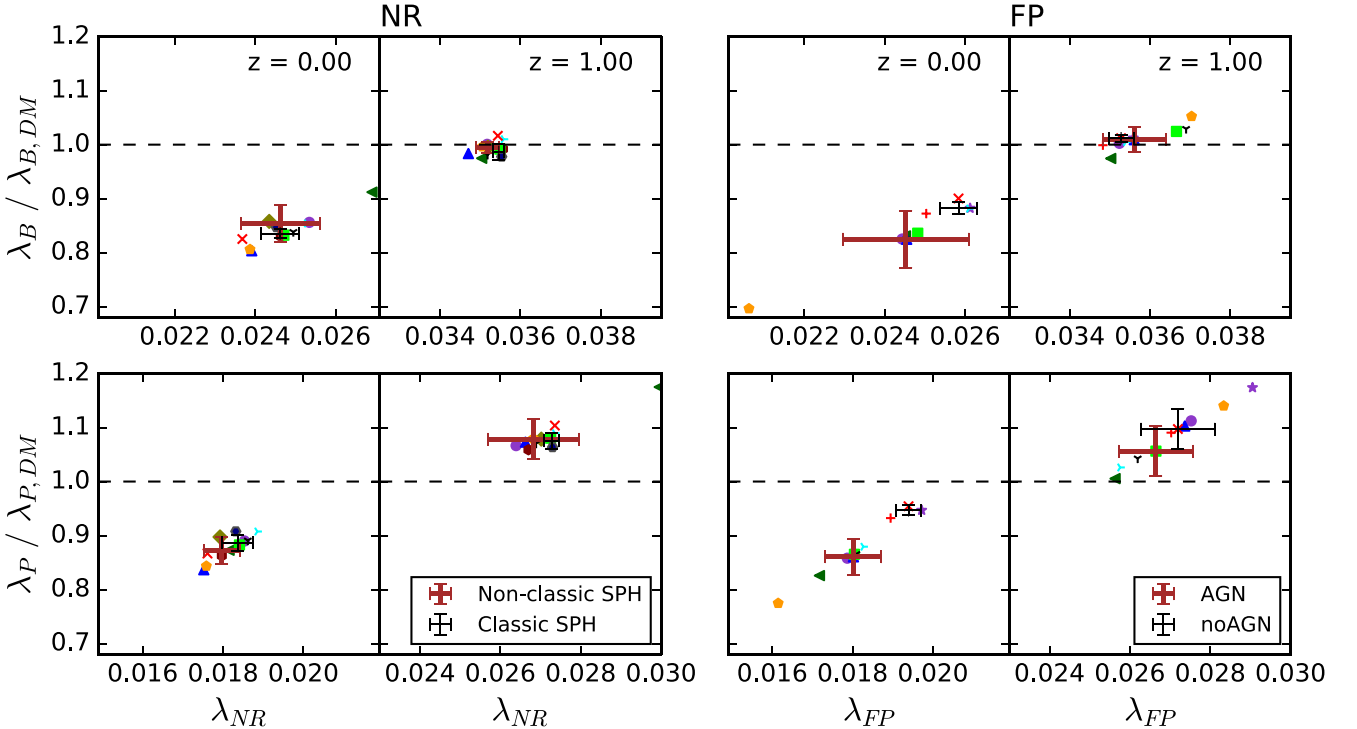
Figure 9. Concentration changes with respect to the DM runs. The left-hand column shows the results from NR runs, while the right-hand column is from the FP runs. The two subplots in each column show the results at both $z = 0$ and $z = 1$, which is indicated in the top left of each panel. The coloured symbols represent the different simulation codes, as indicated on Fig. 6. Again, the NR runs are separated into non-classic and classic SPH subgroups, while the FP runs are separated into AGN and noAGN subgroups, as indicated by the error bars in the legends.

Figure 10. Spin parameter changes with respect to the DM runs. The left-hand column shows the results from NR runs, while the right-hand column is for the FP runs. The two different methods (indicated as λ_B (Bullock et al. 2001), λ_P (Peebles 1969), in the *y*-label) are shown in each row. There are two subplots for each panel, which show the results at the two redshifts as indicated in the uppermost panels. The coloured symbols represent the different simulation codes, as indicated on Fig. 6. Again, we separate the NR runs into non-classic SPH and classic SPH subgroups, the FP runs into AGN and noAGN subgroups, as indicated by the error bars in the legends.

isodensity surfaces to verify our results, which we describe in Appendix C.

In Fig. 11, we show how the axis ratios, b/a and c/a, change between the DM runs and the corresponding NR and FP runs (left-hand and right-hand columns) within thin isodensity and isopotential shells (upper and lower panels) at R_{2500}, R_{500}, and R_{200} (left-hand, middle, and right-hand panels within each column) as a function of b/a and c/a in the NR and FP runs; the relevant redshift is shown in the leftmost panel of each row.

Broadly similar trends are evident in both the NR and FP runs at both redshifts. At $z = 0$, the isopotential shells become slightly

rounder at all radii, by a factor of ∼1.1–1.2. The outermost isodensity shell becomes slightly rounder by a similar factor; the inner shells become more oblate, with negligible change in c/a, but b/a drops by a factor of ∼0.8. At $z = 1$, the trend is such that the inner isodensity shells become slightly rounder by a factor of ∼1.1 in both the NR and FP runs, whereas the outermost shell can be either more oblate (NR) or prolate (FP). The isopotential shells change in such a way that c/a is enhanced whereas b/a is reduced, resulting in negligible net change in the overall shape of the halo.

The effect of including baryonic physics on the shapes of dark matter haloes has been studied previously with hydrodynamic
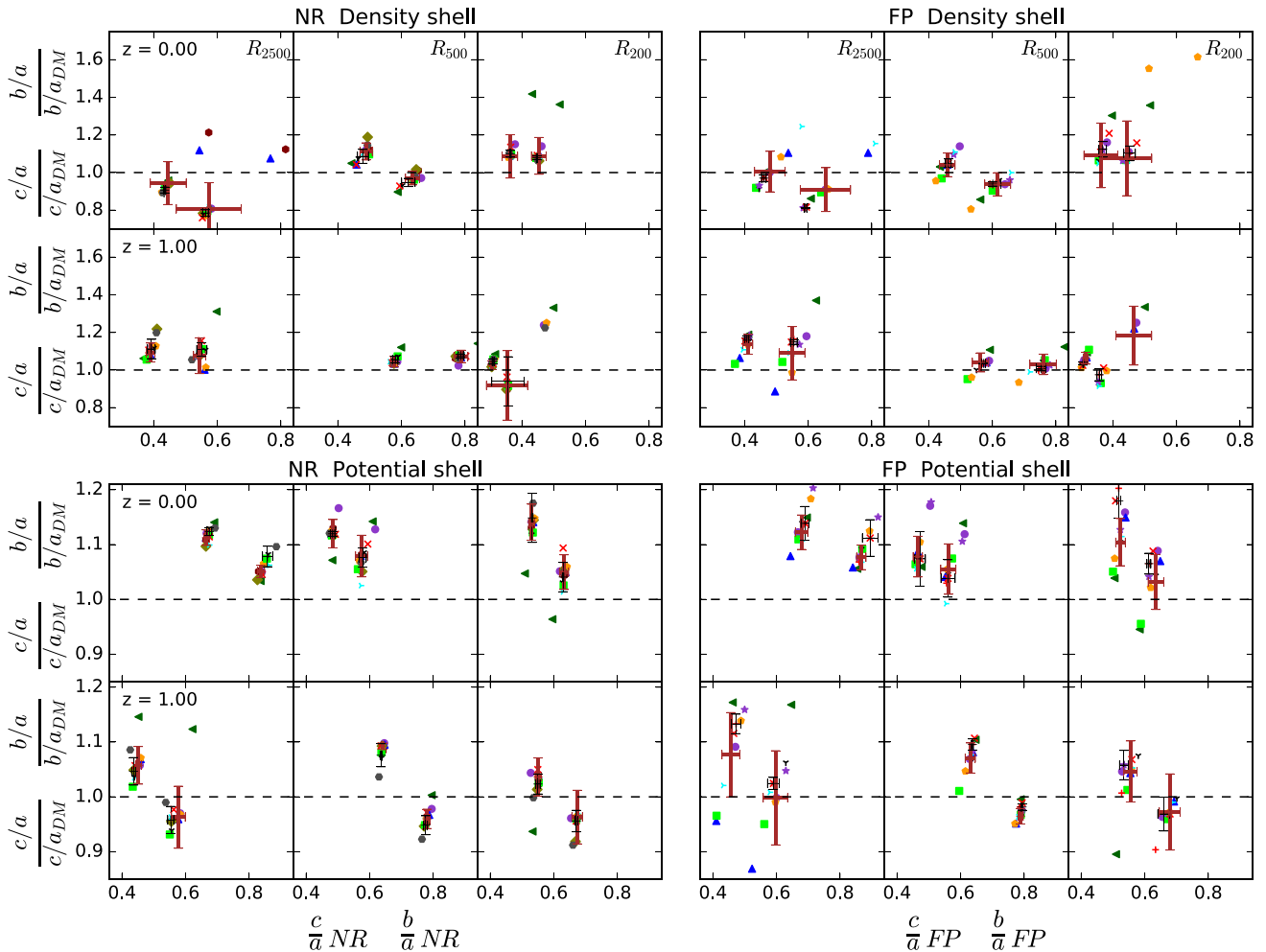
Figure 11. The halo shape (axis ratios: $\frac{c}{a}$ and $\frac{b}{a}$) changes between the DM runs and NR runs (left-hand column)/FP runs (right-hand column) from both the isodensity shells (top two panels) and the isopotential shells (lower two panels). These results are calculated through the inertia method. We refer to Fig. 6 for the meanings of the coloured symbols. Inside each panel, we show the results at three shells at R_{2500}, R_{500}, and R_{200} from left to right within each subplot, and at redshifts of $z = 0$ and $z = 1$ in the top and bottom subplots. Again, the error bars from the FP runs are grouped into AGN (brown thick error bars) and noAGN (black thin error bars); while the error bar from the NR runs are grouped into non-classic SPH (brown thick error bars) and classic SPH (black thin error bars) methods.

simulations in Kazantzidis et al. (2004), Knebe et al. (2010), Bryan et al. (2013), Tenneti et al. (2014), Butsky et al. (2015), and Velliscig et al. (2015), etc. Kazantzidis et al. (2004) found that haloes formed in simulations with gas cooling are significantly more spherical than corresponding haloes formed in adiabatic simulations. Knebe et al. (2010) found that the inclusion of gas physics has no affect on the (DM) shapes of subhaloes, but an influence on their suite of host haloes, which drives the DM halo to become more spherical especially at the central regions (see also Debattista et al. 2008; Abadi et al. 2010; Tissera et al. 2010; Bryan et al. 2013; Tenneti et al. 2014; Butsky et al. 2015; Tenneti et al. 2015, etc.). Our results from the isopotential shell are in agreement with these literatures. However, at the most inner isodensity shell – R_{2500}, there is a decrease of b/a (slightly smaller decrease for c/a). However, the increases for both b/a and c/a at R_{2500} are very clear from the isopotential shell. This is possibly caused by the substructures in the isodensity shell, which has less effect with the isopotential shell method. Using hydrodynamical simulations with different versions of baryon models, Velliscig et al. (2015) showed these different baryon models have less effect on the halo shape. This agrees with our findings

from Fig. 11, which shows a broadly agreement between different simulation codes as well as between the NR and FP runs.

5.6 Velocity anisotropy

We finish our analysis by looking at the velocity anisotropy

$$\beta = 1 - \frac{\sigma_{\tan}^2}{2\sigma_{\rm r}^2},\tag{7}$$

where $\sigma_{\tan}$ and $\sigma_{\rm r}$ are the tangential and radial velocity dispersions. We compute these components of the velocity dispersion using the particles selected in the isopotential shells at the three radii, and show the results in Fig. 12, revealing how β varies between NR and FP runs (left-hand and right-hand columns) at $z = 0$ and 1 (upper and lower rows within each column) at R_{2500}, R_{500}, and R_{200} (left-hand, middle, and right-hand panels within each column).

Again, we see very similar values and changes of the β parameter between the NR and FP runs at fixed radius and redshift. At redshift $z = 1$, we have larger β values at R_{200} and R_{2500} than at R_{500}; while at $z = 0$ the β value is much larger at R_{500} than at the other two radii.
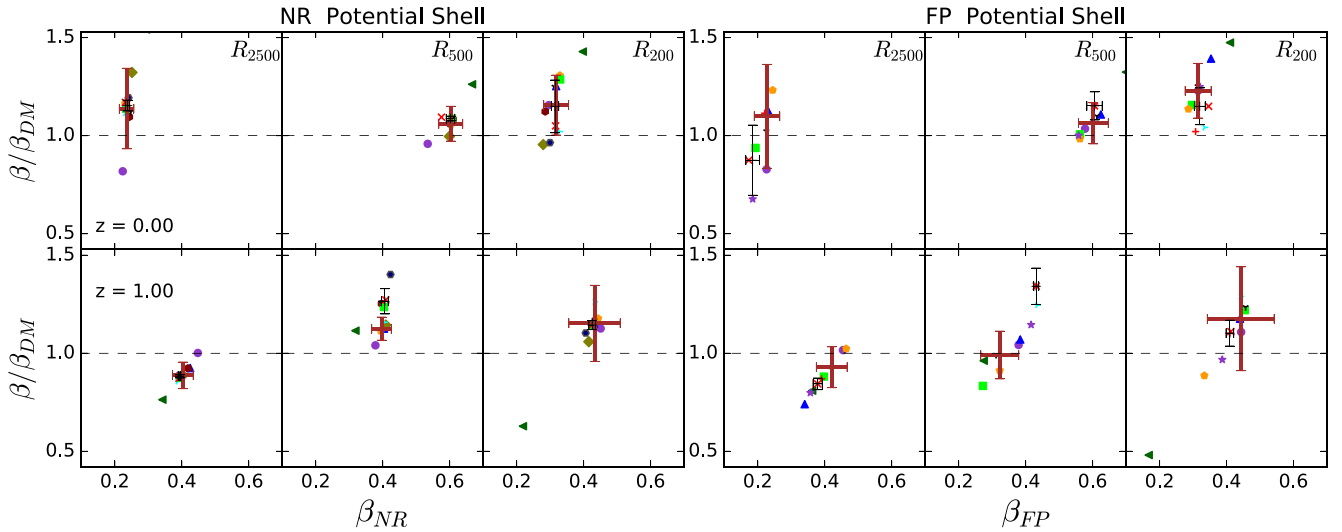
Figure 12. The halo velocity anisotropy, β. The difference between the DM runs and NR runs (left-hand column)/FP runs (right-hand column). This figure is very similar to Fig. 11 in subplot distribution, symbols and error bars. We refer to Fig. 11 for more details.

The incrementation of β at R_{200} is ~ 10 per cent at both redshifts; at R_{500}, there is a slightly small increase of β (~ 5 per cent) at $z = 0$, while there are large disagreements between the subgroups at $z = 1$; at the innermost radius R_{2500}, there are about 10 per cent increase of β at $z = 0$, but about 10 per cent decrease of β at $z = 1$ compared to their DM runs. Similar to the halo shape changes, we do not find a clear separation between these subgroups, except the ones at R_{500} and $z = 1$. There are also broad agreements between the results from the isodensity and from the isopotential shells.

Lau et al. (2010) investigated two hydrodynamical simulations: one with NR gas; the other including gas cooling, star formation, and feedback. By comparing the two, they found that the dark matter velocity anisotropy profile is almost unaffected by the addition of cooling, star formation and feedback and insensitive to redshift between $z = 0$ and 1. This is in very good agreement with what we find in Fig. 12 – there are very similar values and changes of the β parameter between the NR and FP runs.

6 DISCUSSION AND CONCLUSIONS

We have investigated the performance of 11 modern astrophysical simulation codes – HYDRA, AREPO, RAMSES, and eight versions of GADGET with different SPH implementations – and with different baryonic models – by carrying out cosmological zoom simulations of a single massive galaxy cluster. By comparing different simulation codes and different runs ranging from DM to FP runs, which incorporate cooling, star formation, BH growth, and various forms of feedback, we set out to

(i) quantify the scatter between codes and different baryon models.

(ii) understand the impact of baryons on cluster properties, and the extent to which these properties converge.

For clarity, and motivated by the results of Paper I, we grouped codes according to whether or not they are 'Classic SPH', which produce declining entropy profiles with decreasing radius in NR runs, or 'non-Classic SPH', which include the mesh, moving mesh, and modern SPH codes, which recover entropy cores at small radii. We also grouped FP runs according to whether or not they include

BH growth and AGN feedback as 'AGN' and 'noAGN' runs, respectively. Our key findings can be summarized as follows.

Code scatter: in Paper I, we already saw that code-to-code scatter between codes for the aligned DM runs is within 5 per cent for the total mass profile. If we ignore this difference, the NR gas boosts this scatter up to ~ 30 per cent at $z = 0$, with the largest difference evident in the central regions, and up to ~ 50 per cent at $z = 1$. However, by grouping codes into classic and non-classic SPH, the scatter for the total mass profile within a grouping is reduced to ~ 20 per cent; this means that the disagreement is driven by the approach to solving the equations of gas dynamics. The scatter for the total density profile is reduced to ≤ 5 per cent between all codes at $R \geq R_{2500}$, and even smaller at larger radius.

The scatter in the total mass profile between different codes in the FP runs, when compared to the NR runs, is larger – over 100 per cent at $z = 0$, greater at $z = 1$, within the central regions. Grouping the runs into those that include AGN feedback and those that do not, the scatter in the central regions is still substantial, which implies that the complexities of subgrid physics can produce very different results, even when similar baryonic physics prescriptions are adopted. This is especially true for the codes with AGN feedback. The scatter between different runs reduces to ≤ 10 per cent at $R \approx R_{2500}$, and smaller at larger radii.

For most of the global cluster properties investigated in this paper, we find the scatter between different codes and different baryonic physics models is within ~ 20 per cent, in agreement with Paper I, Paper II, and Paper III.

Impact of baryons: using the DM runs as our reference, we find that the change in total mass profile in the FP runs is more marked than in the NR runs, especially within the central regions. Already within R_{500} we see ~ 10 per cent variations with respect to the median in the FP runs, which grows to ~ 20 per cent variations at R_{2500}. In contrast, the variations with respect to the median are markedly smaller in the NR runs, $\lesssim 10$ per cent at R_{2500}. The impact on the central density appears to be redshift-, code-, and physics-dependent, in so far as we see a largely uniform trend for lower central densities in the NR runs at $z = 0$; enhanced central densities in the FP runs at $z = 1$; and a mixture of behaviours in the NR and FP runs at $z = 1$ and 0, respectively, although it is noteworthy

that it is the non-classic SPH and AGN that produce lower central densities, as we might expect. Overall, we conclude that the scatter between the codes in the NR runs is less important than the scatter between different baryonic physics models in the FP runs.

Although the different global cluster properties have different responses to baryon physics, there is broad agreement at both redshifts between the NR and FP runs, and with the conclusions of Paper II. Because of the large scatter of the total mass profile in the central regions, the total inner density slope γ and the concentration C_{NFW}, shows the largest scatter, with a clear separation between the different subgroups at $z = 0$.

By choosing the three characteristic radii – R_{2500}, R_{500}, and R_{200}, we investigate how the cluster properties change at different radii. The halo mass changes have a clear radius dependence at both redshifts, the inner radius shows the largest increase for both the NR and FP runs compared to the DM runs. There is almost no mass change for M_{200} at both redshifts. The halo shape changes are dependent on the choice of the shells; isodensity shells change from inner to outer radii, but are weakly dependent on redshift, whereas isopotential shell changes are systematic with radius and redshift.

It is interesting to note that the clear separation we see between classic and non-classic SPH runs in the mass profiles in the NR runs is not reproduced in the FP runs. How much of this difference is driven by the hydrodynamical technique? In the AGN runs (right-upper panel of Fig. 3), the classic SPH codes G2-x and G3-owls tend to have much higher density at the cluster centre than the non-classic SPH codes G3-x, arepo, and ramses, while the non-classic SPH codes G3-pesph, which uses a heuristic model to quench star formation, produces a much lower density profile than the other codes from the noAGN group. In addition, the gas profile difference between these simulation codes in the NR runs is about 100 per cent at the cluster centre, as was shown in Paper I. This seems to suggest that the hydrodynamic technique can be as important as baryonic physics in setting the mass profile in the FP runs. However, we note also that the total mass profile in the non-classic SPH code – arepo-sh – that does not include AGN feedback is very close to the classic SPH codes without AGN feedback, and the non-classic SPH code G3-magneticum has a higher central density than codes that do not include AGN feedback, despite having AGN feedback included. This suggests that the hydrodynamic scheme may be important, but the details of the baryonic physics prescription is more important in shaping the mass profile.

There are two FP runs of G3-music in this study, the original one runs with gadget-3 code and the Springel & Hernquist (2002) baryon model; while the other one – G2-musicpi run with gadget code and the Piontek & Steinmetz (2011) baryon model. Through this study, we find that there is almost no difference between the two simulations, which can be understood as there are no differences between the two simulation codes and between the two versions of baryon models for this simulated galaxy cluster.

Although we have shown the scatter between different simulation codes/techniques and between different baryonic models, a detailed comparison of the algorithms as well as of the numerical implementation methods of baryonic models is in great needs, because these details are essential for explaining the scatter we show in this paper. To achieve this goal, we are planning to first perform a convergence test in a following study, and then extend this comparison project to an extensive examination on these parameters in the baryon models.

Although this work is based on the analysis of only one simulated galaxy cluster, we argue that our results are robust, because most of them are mainly shown by the differences, in which most systematic errors should be canceled. However, it will be worth to increase the statistics by simulating more clusters in further comparisons: for example, relaxed and un-relaxed clusters may give different answers due to their different dynamical state. We are including more MUSIC clusters to our comparison project and will present the results in future papers.

run on the CFI-NSRIT funded Saint Mary's Computational Astrophysics Laboratory.

The authors contributed to this paper in the following ways: WC, CP, and AK formed the core team that organized and analysed the data, made the plots and wrote the paper. CP, WC, LO, AK, MK, FRP, and GY organized the nIFTy workshop at which this programme was completed. GY supplied the initial conditions. PJE assisted with the analysis. All the other authors, as listed in Section 2 performed the simulations using their codes. All authors read and comment on the paper.

The simulation used for this paper has been run on Marenostrum supercomputer and is publicly available at the MUSIC website.

The AREPO simulations were performed with resources awarded through STFCs DiRAC initiative.

G3-SPHS sumulations were carried out using resources provided by the Pawsey Supercomputing Centre with funding from the Australian Government and the Government of Western Australia.

G3-PESPH simulations were carried out using resources at the Center for High Performance Computing in Cape Town, South Africa.

G2-ANARCHY simulations were performed on the Teide High-Performance Computing facilities provided by the Instituto Tecnológico y de Energías Renovables (ITER, SA).

This research has made use of NASA's Astrophysics Data System (ADS) and the arXiv preprint server.

All the figures in this paper are plotted using the PYTHON MATPLOTLIB package (Hunter 2007).

REFERENCES

Abadi M. G., Navarro J. F., Fardal M., Babul A., Steinmetz M., 2010, MNRAS, 407, 435
Angulo R. E., Baugh C. M., Frenk C. S., Bower R. G., Jenkins A., Morris S. L., 2005, MNRAS, 362, L25
Aubert D., Teyssier R., 2010, ApJ, 724, 244
Balaguera-Antolínez A., Porciani C., 2013, J. Cosmol. Astropart. Phys., 4, 22
Beck A. M. et al., 2016, MNRAS, 455, 2110
Bett P., Eke V., Frenk C. S., Jenkins A., Helly J., Navarro J., 2007, MNRAS, 376, 215
Biffi V., Sembolini F., De Petris M., Valdarnini R., Yepes G., Gottlöber S., 2014, MNRAS, 439, 588
Bocquet S., Saro A., Dolag K., Mohr J. J., 2016, MNRAS, 456, 2361
Booth C. M., Schaye J., 2009, MNRAS, 398, 53
Borgani S., Kravtsov A., 2011, Adv. Sci. Lett., 4, 204
Bryan S. E., Kay S. T., Duffy A. R., Schaye J., Dalla Vecchia C., Booth C. M., 2013, MNRAS, 429, 3316
Bullock J. S., Dekel A., Kolatt T. S., Kravtsov A. V., Klypin A. A., Porciani C., Primack J. R., 2001, ApJ, 555, 240
Butsky I. et al., 2015, preprint (arXiv:1503.04814)
Chan T. K., Kereš D., Oñorbe J., Hopkins P. F., Muratov A. L., Faucher-Giguère C.-A., Quataert E., 2015, MNRAS, 454, 2981
Churazov E., Sazonov S., Sunyaev R., Forman W., Jones C., Böhringer H., 2005, MNRAS, 363, L91
Couchman H. M. P., Thomas P. A., Pearce F. R., 1995, ApJ, 452, 797
Cui W., Borgani S., Dolag K., Murante G., Tornatore L., 2012, MNRAS, 423, 2279
Cui W. et al., 2014a, MNRAS, 437, 816
Cui W., Borgani S., Murante G., 2014b, MNRAS, 441, 1769
Cui W. et al., 2016, MNRAS, 456, 2566
Cusworth S. J., Kay S. T., Battye R. A., Thomas P. A., 2014, MNRAS, 439, 2485
Dalla Vecchia C., Schaye J., 2008, MNRAS, 387, 1431
Davé R., Katz N., Oppenheimer B. D., Kollmeier J. A., Weinberg D. H., 2013, MNRAS, 434, 2645
Debattista V. P., Moore B., Quinn T., Kazantzidis S., Maas R., Mayer L., Read J., Stadel J., 2008, ApJ, 681, 1076

Dehnen W., Aly H., 2012, MNRAS, 425, 1068
Di Cintio A., Brook C. B., Macciò A. V., Stinson G. S., Knebe A., Dutton A. A., Wadsley J., 2014a, MNRAS, 437, 415
Di Cintio A., Brook C. B., Dutton A. A., Macciò A. V., Stinson G. S., Knebe A., 2014b, MNRAS, 441, 2986
Dolag K., Jubelgas M., Springel V., Borgani S., Rasia E., 2004, ApJ, 606, L97
Dolag K., Vazza F., Brunetti G., Tormen G., 2005, MNRAS, 364, 753
Dolag K., Gaensler B. M., Beck A. M., Beck M. C., 2015, MNRAS, 451, 4277
Duffy A. R., Schaye J., Kay S. T., Dalla Vecchia C., Battye R. A., Booth C. M., 2010, MNRAS, 405, 2161
Elahi P. J. et al., 2016, MNRAS, 458, 1096
Fabjan D., Borgani S., Tornatore L., Saro A., Murante G., Dolag K., 2010, MNRAS, 401, 1670
Fabjan D., Borgani S., Rasia E., Bonafede A., Dolag K., Murante G., Tornatore L., 2011, MNRAS, 416, 801
Fedeli C., 2012, MNRAS, 424, 1244
Ferland G. J., Korista K. T., Verner D. A., Ferguson J. W., Kingdon J. B., Verner E. M., 1998, PASP, 110, 761
Frenk C. S. et al., 1999, ApJ, 525, 554
Gill S. P. D., Knebe A., Gibson B. K., 2004, MNRAS, 351, 399
Gnedin O. Y., Kravtsov A. V., Klypin A. A., Nagai D., 2004, ApJ, 616, 16
Haardt F., Madau P., 1996, ApJ, 461, 20
Haardt F., Madau P., 2001, in Neumann D. M., Tran J. T. V., eds, XXIst Moriond Astrophysics Meeting, Clusters of Galaxies and the High Redshift Universe Observed in X-rays. Savoie, France, p. 64
Hayashi E., Navarro J. F., Springel V., 2007, MNRAS, 377, 50
Hirschmann M., Dolag K., Saro A., Bachmann L., Borgani S., Burkert A., 2014, MNRAS, 442, 2304
Hopkins P. F., 2013, MNRAS, 428, 2840
Hunter J. D., 2007, Comput. Sci. Eng., 9, 90
Jing Y. P., Suto Y., 2002, ApJ, 574, 538
Katz N., Weinberg D. H., Hernquist L., 1996, ApJS, 105, 19
Kay S. T., Peel M. W., Short C. J., Thomas P. A., Young O. E., Battye R. A., Liddle A. R., Pearce F. R., 2012, MNRAS, 422, 1999
Kazantzidis S., Kravtsov A. V., Zentner A. R., Allgood B., Nagai D., Moore B., 2004, ApJ, 611, L73
Kennicutt R. C., Jr, 1998, ApJ, 498, 541
Khandai N., Di Matteo T., Croft R., Wilkins S., Feng Y., Tucker E., DeGraf C., Liu M.-S., 2015, MNRAS, 450, 1349
Klypin A., Kravtsov A. V., Bullock J. S., Primack J. R., 2001, ApJ, 554, 903
Knebe A., Libeskind N. I., Knollmann S. R., Yepes G., Gottlöber S., Hoffman Y., 2010, MNRAS, 405, 1119
Knollmann S. R., Knebe A., 2009, ApJS, 182, 608
Komatsu E. et al., 2011, ApJS, 192, 18
Kravtsov A. V., Borgani S., 2012, ARA&A, 50, 353
Lau E. T., Nagai D., Kravtsov A. V., 2010, ApJ, 708, 1419
Le Brun A. M. C., McCarthy I. G., Schaye J., Ponman T. J., 2014, MNRAS, 441, 1270
Lin W. P., Jing Y. P., Mao S., Gao L., McCarthy I. G., 2006, ApJ, 651, 636
Martizzi D., Teyssier R., Moore B., Wentz T., 2012, MNRAS, 422, 3081
Martizzi D., Mohammed I., Teyssier R., Moore B., 2014, MNRAS, 440, 2290
Mitchell N. L., McCarthy I. G., Bower R. G., Theuns T., Crain R. A., 2009, MNRAS, 395, 180
Monaghan J. J., 1997, J. Comput. Phys., 136, 298
Monaghan J. J., Lattanzio J. C., 1985, A&A, 149, 135
Munari E., Biviano A., Borgani S., Murante G., Fabjan D., 2013, MNRAS, 430, 2638
Navarro J. F., Frenk C. S., White S. D. M., 1996, ApJ, 462, 563
Navarro J. F., Frenk C. S., White S. D. M., 1997, ApJ, 490, 493
Newman A. B., Treu T., Ellis R. S., Sand D. J., Nipoti C., Richard J., Jullo E., 2013, ApJ, 765, 24
Peebles P. J. E., 1969, ApJ, 155, 393
Pike S. R., Kay S. T., Newton R. D. A., Thomas P. A., Jenkins A., 2014, MNRAS, 445, 1774
Piontek F., Steinmetz M., 2011, MNRAS, 410, 2625

Planelles S., Borgani S., Fabjan D., Killedar M., Murante G., Granato G. L., Ragone-Figueroa C., Dolag K., 2014, MNRAS, 438, 195
Planelles S., Schleicher D. R. G., Bykov A. M., 2015, Space Sci. Rev., 188, 93
Power C., Navarro J. F., Jenkins A., Frenk C. S., White S. D. M., Springel V., Stadel J., Quinn T., 2003, MNRAS, 338, 14
Power C., Knebe A., Knollmann S. R., 2012, MNRAS, 419, 1576
Power C., Read J. I., Hobbs A., 2014, MNRAS, 440, 3243
Prada F., Klypin A. A., Cuesta A. J., Betancort-Rijo J. E., Primack J., 2012, MNRAS, 423, 3018
Price D. J., 2008, J. Comput. Phys., 227, 10040
Puchwein E., Sijacki D., Springel V., 2008, ApJ, 687, L53
Rafieferantsoa M., Davé R., Anglés-Alcázar D., Katz N., Kollmeier J. A., Oppenheimer B. D., 2015, MNRAS, 453, 3980
Rasera Y., Teyssier R., 2006, A&A, 445, 1
Rasia E., Tormen G., Moscardini L., 2004, MNRAS, 351, 237
Read J. I., Hayfield T., 2012, MNRAS, 422, 3037
Remus R.-S., Burkert A., Dolag K., Johansson P. H., Naab T., Oser L., Thomas J., 2013, ApJ, 766, 71
Sawala T., Frenk C. S., Crain R. A., Jenkins A., Schaye J., Theuns T., Zavala J., 2013, MNRAS, 431, 1366
Schaller M. et al., 2015a, MNRAS, 451, 1247
Schaller M. et al., 2015b, MNRAS, 452, 343
Schaye J., 2004, ApJ, 609, 667
Schaye J., Dalla Vecchia C., 2008, MNRAS, 383, 1210
Schaye J. et al., 2010, MNRAS, 402, 1536
Sembolini F., Yepes G., De Petris M., Gottlöber S., Lamagna L., Comis B., 2013, MNRAS, 429, 323
Sembolini F., De Petris M., Yepes G., Foschi E., Lamagna L., Gottlöber S., 2014, MNRAS, 440, 3520
Sembolini F. et al., 2015, preprint (arXiv:1511.03731) (Paper II)
Sembolini F. et al., 2016, MNRAS, 457, 4063 (Paper I)
Springel V., 2005, MNRAS, 364, 1105
Springel V., 2010, MNRAS, 401, 791
Springel V., Hernquist L., 2002, MNRAS, 333, 649
Springel V., Hernquist L., 2003, MNRAS, 339, 289
Springel V., White S. D. M., Hernquist L., 2004, in Ryder S., Pisano D., Walker M., Freeman K., eds, Proc. IAU Symp. 220, Dark Matter in Galaxies. Astron. Soc. Pac., San Francisco, p. 421
Stanek R., Rudd D., Evrard A. E., 2009, MNRAS, 394, L11
Steinborn L. K., Dolag K., Hirschmann M., Prieto M. A., Remus R.-S., 2015, MNRAS, 448, 1504
Sutherland R. S., Dopita M. A., 1993, ApJS, 88, 253
Tenneti A., Mandelbaum R., Di Matteo T., Feng Y., Khandai N., 2014, MNRAS, 441, 470
Tenneti A., Mandelbaum R., Di Matteo T., Kiessling A., Khandai N., 2015, MNRAS, 453, 469
Teyssier R., 2002, A&A, 385, 337
Teyssier R., Moore B., Martizzi D., Dubois Y., Mayer L., 2011, MNRAS, 414, 195
Thacker R. J., Couchman H. M. P., 2006, Comput. Phys. Commun., 174, 540
Thomas P. A., Couchman H. M. P., 1992, MNRAS, 257, 11
Tissera P. B., White S. D. M., Pedrosa S., Scannapieco C., 2010, MNRAS, 406, 922
Tornatore L., Borgani S., Dolag K., Matteucci F., 2007, MNRAS, 382, 1050
Tricco T. S., Price D. J., 2013, MNRAS, 436, 2810
Velliscig M., van Daalen M. P., Schaye J., McCarthy I. G., Cacciato M., Le Brun A. M. C., Dalla Vecchia C., 2014, MNRAS, 442, 2641
Velliscig M. et al., 2015, MNRAS, 453, 721
Vera-Ciro C. A., Sales L. V., Helmi A., Frenk C. S., Navarro J. F., Springel V., Vogelsberger M., White S. D. M., 2011, MNRAS, 416, 1377
Viel M., Haehnelt M. G., 2006, MNRAS, 365, 231
Vogelsberger M., Genel S., Sijacki D., Torrey P., Springel V., Hernquist L., 2013, MNRAS, 436, 3031
Vogelsberger M. et al., 2014, MNRAS, 444, 1518
Wadsley J. W., Veeravalli G., Couchman H. M. P., 2008, MNRAS, 387, 427
Warnick K., Knebe A., Power C., 2008, MNRAS, 385, 1859
Wendland H., 1995, Adv. Comput. Math., 4, 389
Wiersma R. P. C., Schaye J., Smith B. D., 2009a, MNRAS, 393, 99
Wiersma R. P. C., Schaye J., Theuns T., Dalla Vecchia C., Tornatore L., 2009b, MNRAS, 399, 574
Zhu Q., Marinacci F., Maji M., Li Y., Springel V., Hernquist L., 2016, MNRAS, 458, 1559

APPENDIX A: SIMULATION CODES

RAMSES (Perret, Teyssier)

RAMSES is based on adaptive mesh refinement (AMR) technique, with a tree-based data structure allowing recursive grid refinements on a cell-by-cell basis. The hydrodynamical solver is based on a second-order Godunov method with the Harten-Lax-van Leer-Contact Riemann solver. For the baryon physics, RAMSES modifies Haardt & Madau (1996) for the gas cooling and heating with metal cooling function of Sutherland & Dopita (1993). The UV background and a self-shielding recipe is based on Aubert & Teyssier (2010). The star formation follows Rasera & Teyssier (2006) with density threshold of $n_* = 0.1\,\mathrm{H\,cm^{-3}}$. The formation of supermassive black hole (SMBH) uses the sink particle technique (Teyssier et al. 2011). The SMBH accretion rate can have a boost factor compared to the Bondi accretion rate (Booth & Schaye 2009). It cannot exceed the instantaneous Eddington limit, however. The AGN feedback used is a simple thermal energy dump with $0.1c^2$ of specific energy, multiplied by the instantaneous SMBH accretion rate.

AREPO (Puchwein)

AREPO employs a TREEPM gravity solver and the hydrodynamic equations are solved with a finite-volume Godunov scheme on an unstructured moving Voronoi mesh (Springel 2010). Detailed descriptions of the galaxy formation models implemented in AREPO-IL can be found in Vogelsberger et al. (2013, 2014). The other FP version (AREPO-SH) of AREPO has the same baryon model as G3-MUSIC.

G2-ANARCHY (Dalla Vecchia)

G2-ANARCHY is an implementation of GADGET-2 (Springel 2005) employing the pressure-entropy SPH formulation derived by Hopkins (2013). G2-ANARCHY uses a purely numerical switch for entropy diffusion similar to the one of Price (2008), but without requiring any diffusion limiter. The kernel adopted is the C^2 function of Wendland (1995) with 100 neighbours, with the purpose of avoiding particle pairing (as suggested by Dehnen & Aly 2012). A FP version of this code is not available yet.

G3-X (Murante, Borgani, Beck)

Based on GADGET-3, an updated version of GADGET, G3-X (Beck et al. 2016) employs a Wendland C^4 kernel with 200 neighbours (cf. Dehnen & Aly 2012), artificial conductivity to promote fluid mixing following Price (2008) and Tricco & Price (2013), but with an additional limiter for gravitationally induced pressure gradients. In the FP run of G3-X, gas cooling is computed for an optically thin gas and takes into account the contribution of metals (Wiersma, Schaye & Smith 2009a), with a uniform UV background (Haardt & Madau 2001). Star formation and chemical evolution are implemented as in Tornatore et al. (2007). Supernova feedback is therefore modelled as kinetic and the prescription of Springel & Hernquist (2003) is followed. AGN feedback follows the model described in Steinborn et al. (2015). It sums up both the AGN mechanical and radiative power, which is a function of the SMBH mass and the accretion rate (Churazov et al. 2005) and gives the resulting energy to the surrounding gas, in form of purely thermal energy.

G3-SPHS (Power, Read, Hobbs)

G3-SPHS is a modification of the standard GADGET-3 code, developed to overcome the inability of classic SPH to resolve instabilities. G3-SPHS uses as an alternative either the High Order Core Triangle (HOCT) kernel with 442 neighbours or the Wendland C4 kernel with 200 neighbours, based on a higher order dissipation switch detector. A FP version of this code is under development.

G3-MAGNETICUM (Saro)

G3-MAGNETICUM is an advanced version of GADGET-3. In the NR version, a higher order kernel based on the bias-corrected, sixth-order Wendland kernel (Dehnen & Aly 2012) with 200 neighbours is included. It also includes a low viscosity scheme to track turbulence (Dolag et al. 2005; Beck et al. 2016) and isotropic thermal conduction with 1/20th *Spitzer* rate (Dolag et al. 2004). For its FP runs, the simulation allows for radiative cooling according to Wiersma et al. (2009a) with metal line cooling from the CLOUDY photoionization code (Ferland et al. 1998), and heating from a uniform time-dependent ultraviolet background (Haardt & Madau 2001). The star formation model is improved from Springel & Hernquist (2003), and it also includes chemical evolution model according to Tornatore et al. (2007). The stellar feedback triggers galactic winds with a velocity of $350 \, \mathrm{km \, s^{-1}}$. The detailed SMBH growth and AGN feedback model is presented in Hirschmann et al. (2014) and Dolag et al. (2015).

G3-PESPH (February, Davé, Katz, Huang)

G3-PESPH is an implementation of GADGET-3 with pressure-entropy SPH (Hopkins 2013) which features special galactic wind models. The SPH kernel is an HOCTS ($n = 5$) B-spline with 128 neighbours. For the FP run, the radiative cooling in this simulation code is described in Katz, Weinberg & Hernquist (1996), with metal lines cooling (Wiersma et al. 2009a) and a uniform ionizing UV background (Haardt & Madau 2001). The star formation in this code is based on Springel & Hernquist (2003). In addition, the heuristic model of Rafieferantsoa et al. (2015), tuned to reproduce the exponential truncation of the stellar mass function, is used to quench star formation in massive galaxies. It uses a highly constrained heuristic model for galactic outflows, described in detail in Davé et al. (2013), which utilizes outflows scalings expected for momentum-driven winds in sizable galaxies, and energy-driven scalings in dwarf galaxies. It does not include AGN feedback in this process.

G3-MUSIC (Yepes)

The original MUSIC runs (G3-MUSIC) were done with the GADGET-3 code, based on the entropy-conserving formulation of SPH (Springel & Hernquist 2002). GADGET-3 employs a spline kernel (Monaghan & Lattanzio 1985) and parametrize artificial viscosity following the model described by Monaghan (1997). G3-MUSIC uses the basic Springel & Hernquist (2003) model without SMBH growth and AGN feedback for its FP runs. In addition, an alternative version of MUSIC performed using the radiative feedbacks described in Piontek & Steinmetz (2011) is presented as G2-MUSICPI, which also does not include SMBH growth and AGN feedback.

G3-OWLS (McCarthy, Schaye)

The G3-OWLS is based on the TREEPM-SPH code GADGET-3, and uses standard entropy-conserving SPH with 48 neighbours for its NR runs. For the FP runs, it includes new sub-grid physics for radiative cooling, star formation, stellar feedback, BH growth, and AGN feedback (see more details in Schaye 2004; Dalla Vecchia & Schaye 2008; Schaye & Dalla Vecchia 2008; Booth & Schaye 2009; Wiersma et al. 2009a; Schaye et al. 2010), also for stellar evolution and mass-loss (see more details in Wiersma et al. 2009b), which is developed as part of the OWLS/cosmo-OWLS projects (Schaye et al. 2010; Le Brun et al. 2014).

G2-X (Kay)

G2-X is a modified version of the GADGET-2 code (Springel 2005), using the TREEPM gravity solver and standard entropy-conserving SPH with 50 neighbours for its NR runs. More details of the baryon model for its FP runs can be found at Pike et al. (2014). Cooling follows the prescription of Thomas & Couchman (1992). Gas is converted to stars at a rate given by the Kennicutt–Schmidt relation (Kennicutt 1998). Star formation follows the method of Schaye & Dalla Vecchia (2008). A prompt thermal Type II SNe feedback model is used. The AGN feedback uses the Booth & Schaye (2009) model with a variation.

HYDRA (Thacker)

HYDRA-OMP (HYDRA; Thacker & Couchman 2006), a parallel implementation of the HYDRA code of Couchman et al. (1995), adopts a 'classic' SPH implementation with 52 neighbours, standard pairwise artificial viscosity, and conservative time-stepping scheme that keeps all particles on the same synchronization. No FP runs is performed in this code.

APPENDIX B: HALO SHAPE: DENSITY AND POTENTIAL SHELLS

Both the density and potential shells at R_{2500}, R_{500}, and R_{200} are used to determine the halo shape through the inertia method. Here, we describe how we select out the density and potential shells consistently (similar to Warnick et al. 2008):

(1) The median density ρ_x and potential Φ_x for the shell at the three radii are calculated from all particles within $0.95 \times R_x \leq r \leq 1.05 \times R_x$, where x indicates the overdensity in [2500, 500, 200]. We have checked the median density and potential between different simulation codes, and find the differences are within 15 per cent.

(2) All particles within the density shell ($[0.95 \times \rho_x, 1.05 \times \rho_x]$) or potential shell ($[0.99 \times \Phi_x, 1.01 \times \Phi_x]$) are selected. A smaller range is used for the potential shell, because the potential is much smoother than the density. We adopt a range in density and potential that is twice as large as $z = 1$, to ensure that we have a sufficient number of particles to get a reliable estimate of shape.

(3) All the selected particles are grouped by a Friend-of-Friend (FoF) method with a large linking length of 50 h^{-1} kpc. We use an even larger linking length of 100 h^{-1} kpc for shells at R_{200}, because the particles at this radius have larger separation. The most massive FoF group is chosen. This procedure allows us to remove particles that are too far away from the shell. We have checked the number fraction of the most massive group, which is always larger than 80 per cent of the total selected shell particles.

It is well known that the reliability of shape estimates of particle distributions depends on the number of particles used to trace those distributions (e.g. Tenneti et al. 2014). We have checked the total number of particles selected from these shells, and confirm that none have fewer than 6000 particles.
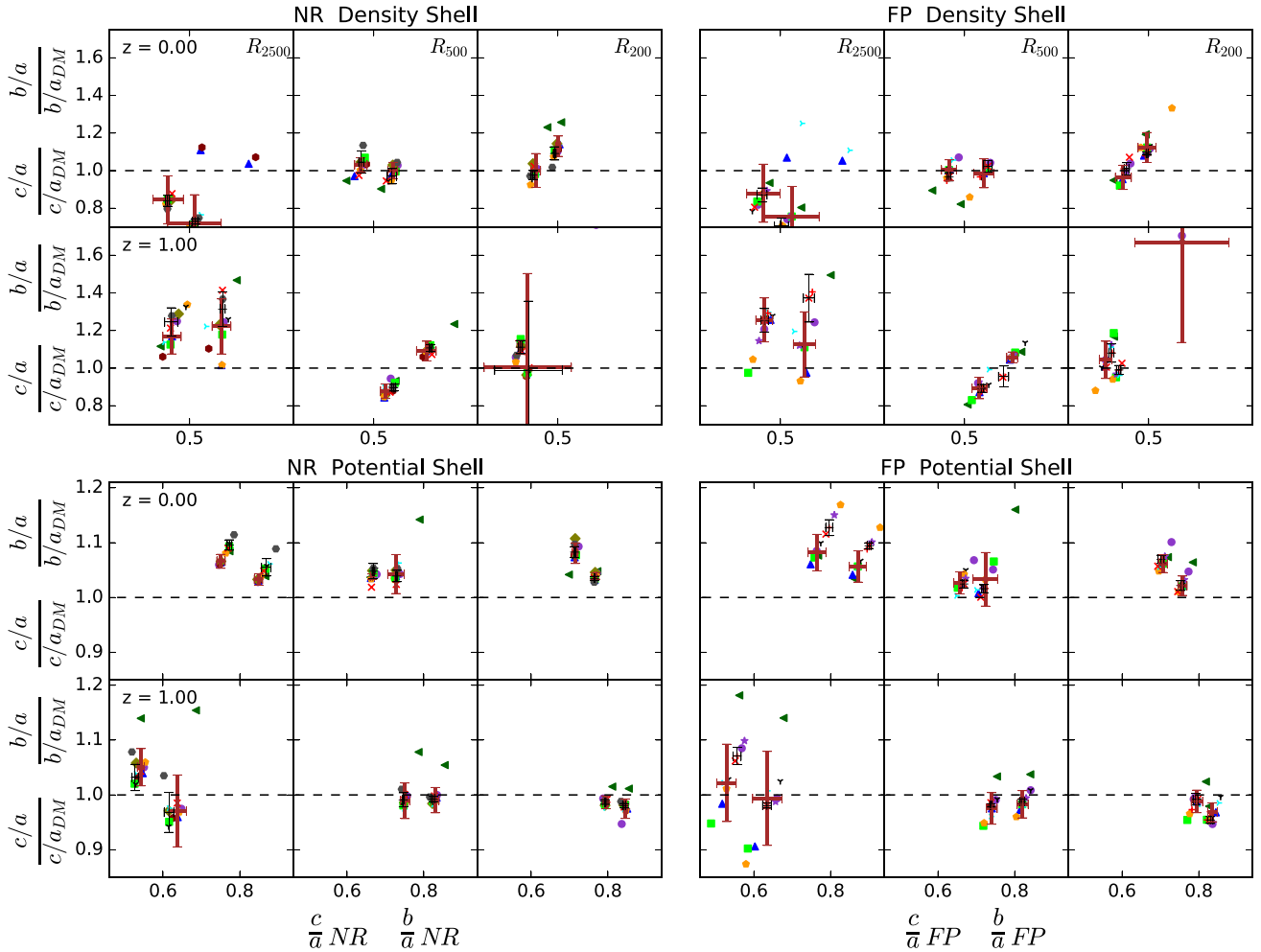
Figure C1. Similarly to Fig. 11, but for the results from the fitting method. Refer to Fig. 11 for the details.

APPENDIX C: HALO SHAPE: DIRECT LINEAR LEAST-SQUARES FITTING METHOD

To investigate the sensitivity of our results on how the halo shape changes between the DM, NR, and FP runs, we recompute halo shapes using a different method, based on a direct linear least-squares fit,[4] to fit ellipsoids to the 3D isodensity surfaces. This fitting method uses the same particles from both density and potential shells for the inertia method. We note here that all particles inside the shell are treated equally during the fitting, i.e. there is no mass weighting. With this fitting method, we can directly estimate the length of the three axes: a, b, and c.

In Fig. C1, we show how the halo shape changes (b/a and c/a) in the NR runs (left-hand column) and FP runs (right-hand column), focusing on three shells corresponding to R_{2500}, R_{500}, and R_{200} (from left to right) as a function of b/a and c/a; results for redshift $z = 0$ (1) are shown in the top (bottom) panels. The top (bottom) two rows show results for the density (potential) shells. We refer to Fig. 6 for the meanings of the colour symbols and error bars. In each panel, we show both c/a and b/a data.

The values of b/a, c/a, and their changes with respect to the DM runs are similar to the results in the corresponding panels in Fig. 11. However, it is worth to note that for the isopotential shell, the fitting method gives slightly smaller changes of both b/a and c/a at $z = 0$; there is almost no change of both b/a and c/a at $z = 1$ and at $R_{500, 200}$; we also expect there are slight variations in the size of the error bars. Besides that, We expect both methods are robust and precise for estimating the halo shape.

[1] *ICRAR, University of Western Australia, 35 Stirling Highway, Crawley, WA 6009, Australia*

[2] *ARC Centre of Excellence for All-Sky Astrophysics (CAASTRO) WA 6009, Australia*

[3] *Departamento de Física Teórica, Módulo 8, Facultad de Ciencias, Universidad Autónoma de Madrid, E-28049 Madrid, Spain*

[4] *Astro-UAM, UAM, Unidad Asociada CSIC, E-28049 Madrid, Spain*

[5] *Jodrell Bank Centre for Astrophysics, School of Physics and Astronomy, The University of Manchester, Manchester M13 9PL, UK*

[6] *Sydney Institute for Astronomy, University of Sydney, Sydney, NSW 2016, Australia*

[7] *School of Physics and Astronomy, University of Nottingham, Nottingham NG7 2RD, UK*

[8] *Physics Department, University of the Western Cape, Cape Town 7535, South Africa*

[9] *University Observatory Munich, Scheinerstr. 1, D-81679 Munich, Germany*

[4] Details of the fitting procedure can be found at here: http://www.mathworks.com/matlabcentral/fileexchange/24693-ellipsoid-fit.

[10]*Instituto de Astrofísica de Canarias, C/Vía Láctea s/n, E-38205 La Laguna, Tenerife, Spain*

[11]*Departamento de Astrofísica, Universidad de La Laguna, Av. del Astrofísico Francisco Sánchez s/n, E-38206 La Laguna, Tenerife, Spain*

[12]*Physics Department, University of Western Cape, Bellville, Cape Town 7535, South Africa*

[13]*South African Astronomical Observatory, PO Box 9, Observatory, Cape Town 7935, South Africa*

[14]*African Institute of Mathematical Sciences, Muizenberg, Cape Town 7945, South Africa*

[15]*Center for High Performance Computing, CSIR Campus, 15 Lower Hope Street, Rosebank, Cape Town 7701, South Africa*

[16]*Astronomy Department, University of Massachusetts, Amherst, MA 01003, USA*

[17]*Department of Physics, Institute for Astronomy, ETH Zurich, Wolfgang-Pauli-Strasse 16, CH-8093 Zurich, Switzerland*

[18]*Astrophysics Research Institute, Liverpool John Moores University, 146 Brownlow Hill, Liverpool L3 5RF, UK*

[19]*INAF – Osservatorio Astronomico di Trieste, via G.B. Tiepolo 11, I-34143 Trieste, Italy*

[20]*Centre for Theoretical Astrophysics and Cosmology, Institute for Computational Science, University of Zurich, Winterthurerstrasse 190, CH-8057 Zurich, Switzerland*

[21]*Institute of Astronomy and Kavli Institute for Cosmology, University of Cambridge, Madingley Road, Cambridge CB3 0HA, UK*

[22]*Department of Physics, University of Surrey, Guildford, Surrey GU2 7XH, UK*

[23]*Excellence Cluster Universe, Boltzmannstr. 2, D-85748 Garching, Germany*

[24]*Department of Astronomy and Physics, Saint Mary's University, 923 Robie Street, Halifax, Nova Scotia B3H 3C3, Canada*

This paper has been typeset from a TEX/LATEX file prepared by the author.